Electronic Supplementary Material (ESI) for Energy & Environmental Science.
This journal is © The Royal Society of Chemistry 2022

Electronic Supplementary Information

Competitive nucleation and growth behavior in Li-Se batteries

Ji Hyun Um,[a‡] Aihua Jin,[a‡] Xin Huang,[b] Jeesoo Seok,[c] Seong Soo Park,[d] Janghyuk Moon,[d] Mihyun Kim,[a] So Hee Kim,[e] Hyun Sik Kim,[f] Sung-Pyo Cho,[gh] Héctor D. Abruña[c*] and Seung-Ho Yu[a*]

[a]Department of Chemical and Biological Engineering, Korea University, 145 Anam-ro, Seongbuk-gu, Seoul 02841, Republic of Korea
[b]Cornell High Energy Synchrotron Source, Cornell University, Ithaca, New York 14853, USA
[c]Department of Chemistry and Chemical Biology, Cornell University, Ithaca, New York 14853, USA
[d]School of Energy Systems Engineering, Chung-Ang University, 84 Heukseok-ro, Dongjak-gu, Seoul 06974, Republic of Korea
[e]Advanced Analysis Center, Korea Institute of Science and Technology, Seoul 02792, Republic of Korea
[f]Analysis Technical Center, Korea Institute of Ceramic Engineering & Technology, 101 Soho-ro, Jinju-si, Gyeongsangnam-do, Republic of Korea
[g]National Center for Inter-University Research Facilities, Seoul National University, Seoul 08826, Republic of Korea
[h]Graphene Research Center, Advanced Institute of Convergence Technology, Suwon 16229, Republic of Korea

‡These authors contributed equally to this work.
*Corresponding authors: hda1@cornell.edu (H.D.A), seunghoyu@korea.ac.kr (S.-H.Y)

Table of Contents

Supplementary Figures
- Supplementary Fig. 1 ····· 2
- Supplementary Fig. 2 ····· 3
- Supplementary Fig. 3 ····· 5
- Supplementary Fig. 4 ····· 6
- Supplementary Fig. 5 ····· 8
- Supplementary Fig. 6 ····· 9
- Supplementary Fig. 7 ····· 12
- Supplementary Fig. 8 ····· 14
- Supplementary Fig. 9 ····· 15
- Supplementary Fig. 10 ····· 20
- Supplementary Fig. 11 ····· 21
- Supplementary Fig. 12 ····· 23
- Supplementary Fig. 13 ····· 24
- Supplementary Fig. 14 ····· 25
- Supplementary Fig. 15 ····· 26
- Supplementary Fig. 16 ····· 27
- Supplementary Fig. 17 ····· 28
- Supplementary Fig. 18 ····· 29
- Supplementary Fig. 19 ····· 30
- Supplementary Fig. 20 ····· 31
- Supplementary Fig. 21 ····· 33
- Supplementary Fig. 22 ····· 34

Supplementary Table 1 ····· 18

Supplementary Video Captions
- Supplementary Video 1 ····· 35
- Supplementary Video 2 ····· 35
- Supplementary Video 3 ····· 35
- Supplementary Video 4 ····· 35
- Supplementary Video 5 ····· 35
- Supplementary Video 6 ····· 35
- Supplementary Video 7 ····· 35
- Supplementary Video 8 ····· 35

Supplementary References ····· 36

Supplementary Figures

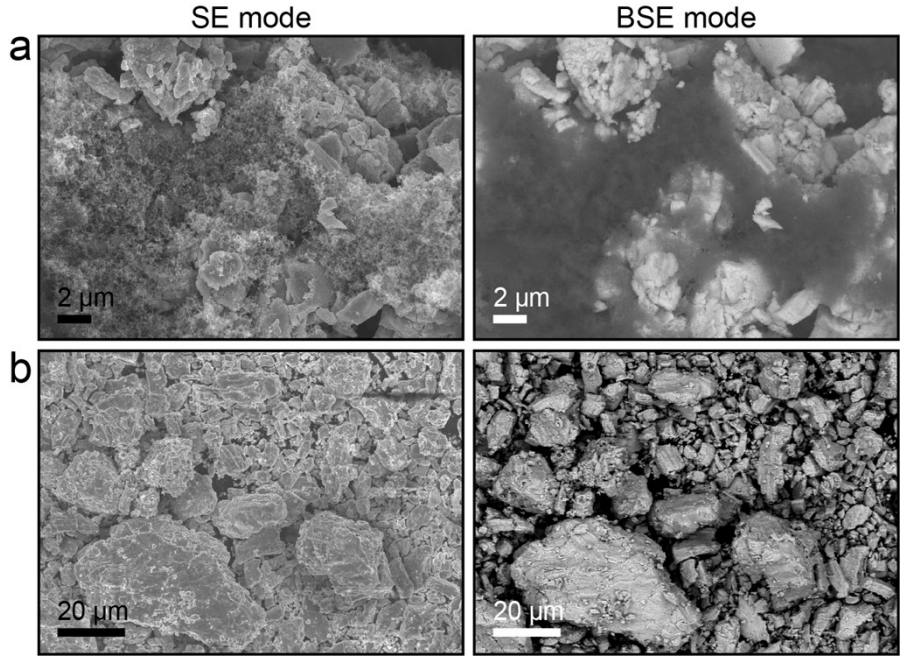

Fig. S1 *Ex-situ* SEM images of (a) pristine Se electrode and (b) commercially available Se powder in secondary electron (SE) and back scattered electron (BSE) modes. The heavier the atomic number, the brighter it is in the BSE image, wherein bright and dark regions in the BSE-SEM of pristine electrode correspond to the Se and the C, respectively. The commercially available Se powder with irregular particle sizes was directly used in this study without any further treatment.

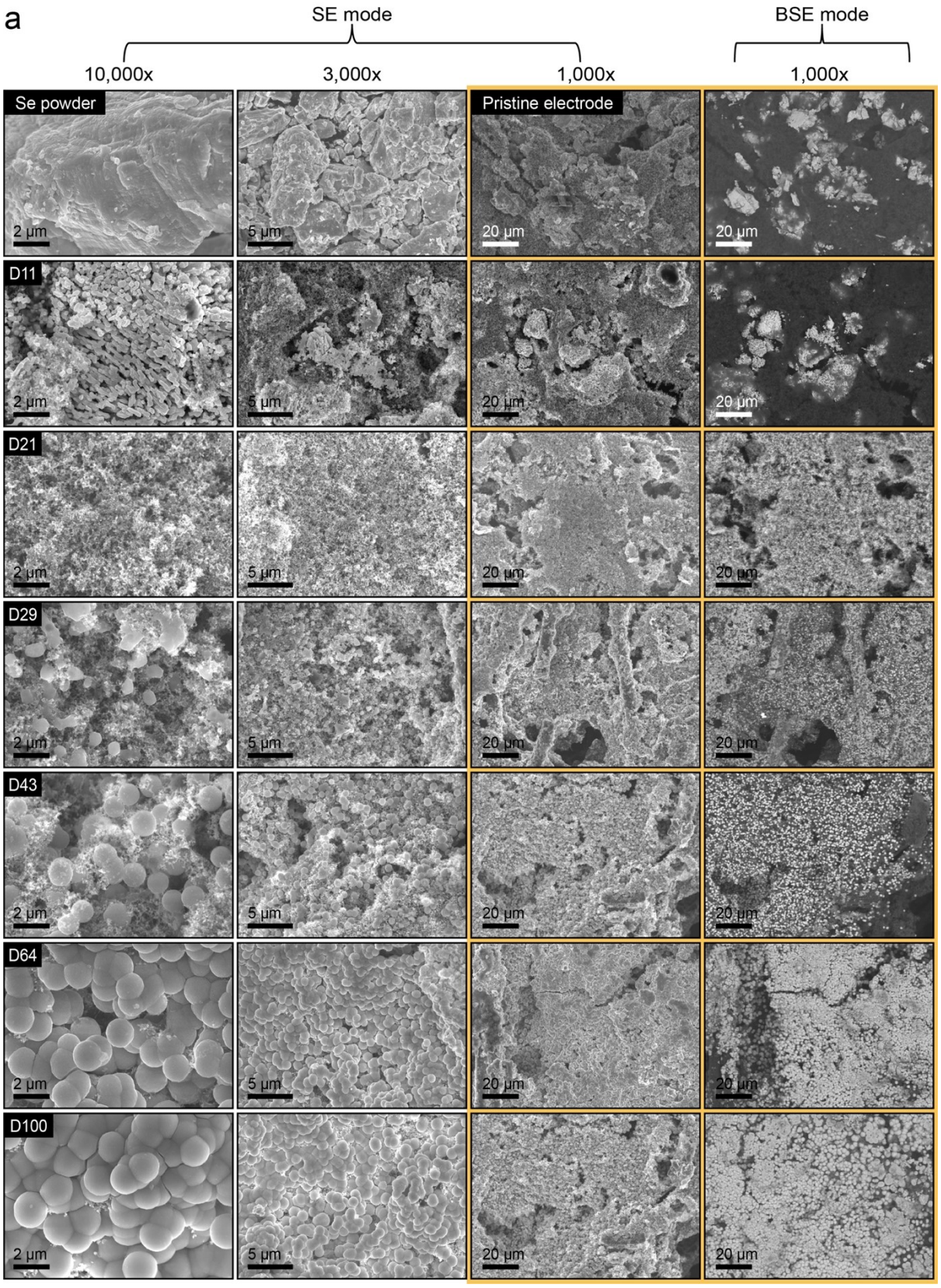
a
SE mode
BSE mode
10,000x
3,000x
1,000x
1,000x
Se powder
Pristine electrode
D11
D21
D29
D43
D64
D100
2 μm
5 μm
20 μm

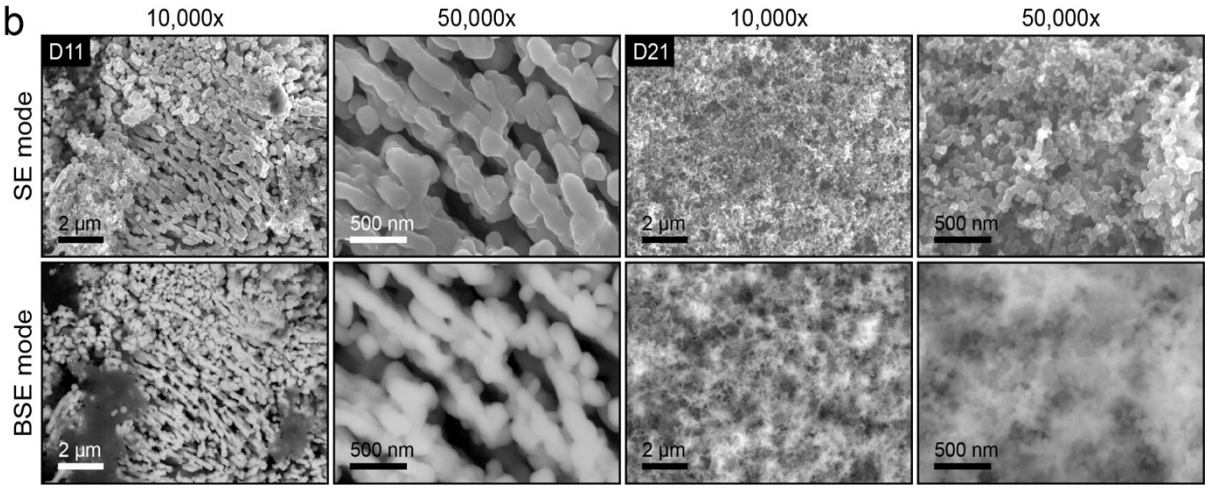

Fig. S2 (a) *Ex-situ* SEM images at the specific DODs in SE and BSE modes. (b) SEM images at D11 and D21 in SE and BSE modes. The dissolving Se until D21 is confirmed by BSE-SEM.

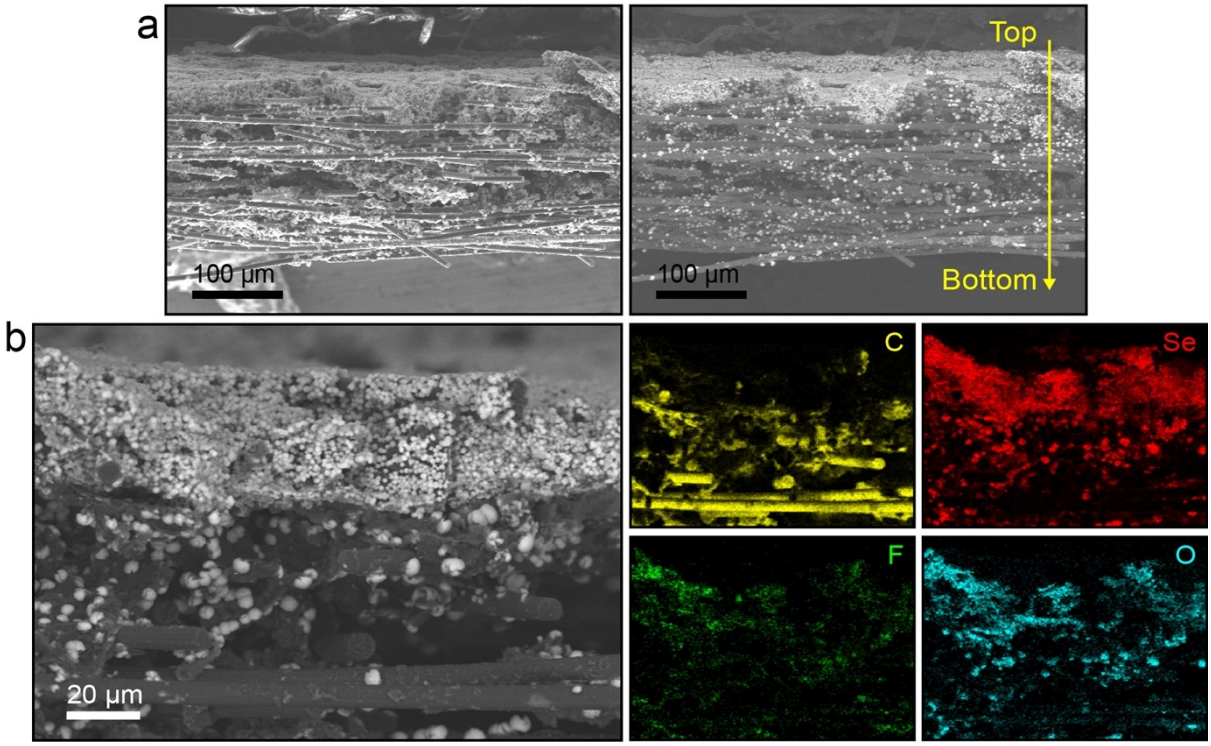

Fig. S3 (a) Cross-sectional SEM images of Se electrode at D100 in SE (left) and BSE (right) modes. (b) EDX mapping of cross-sectional Se electrode at D100.

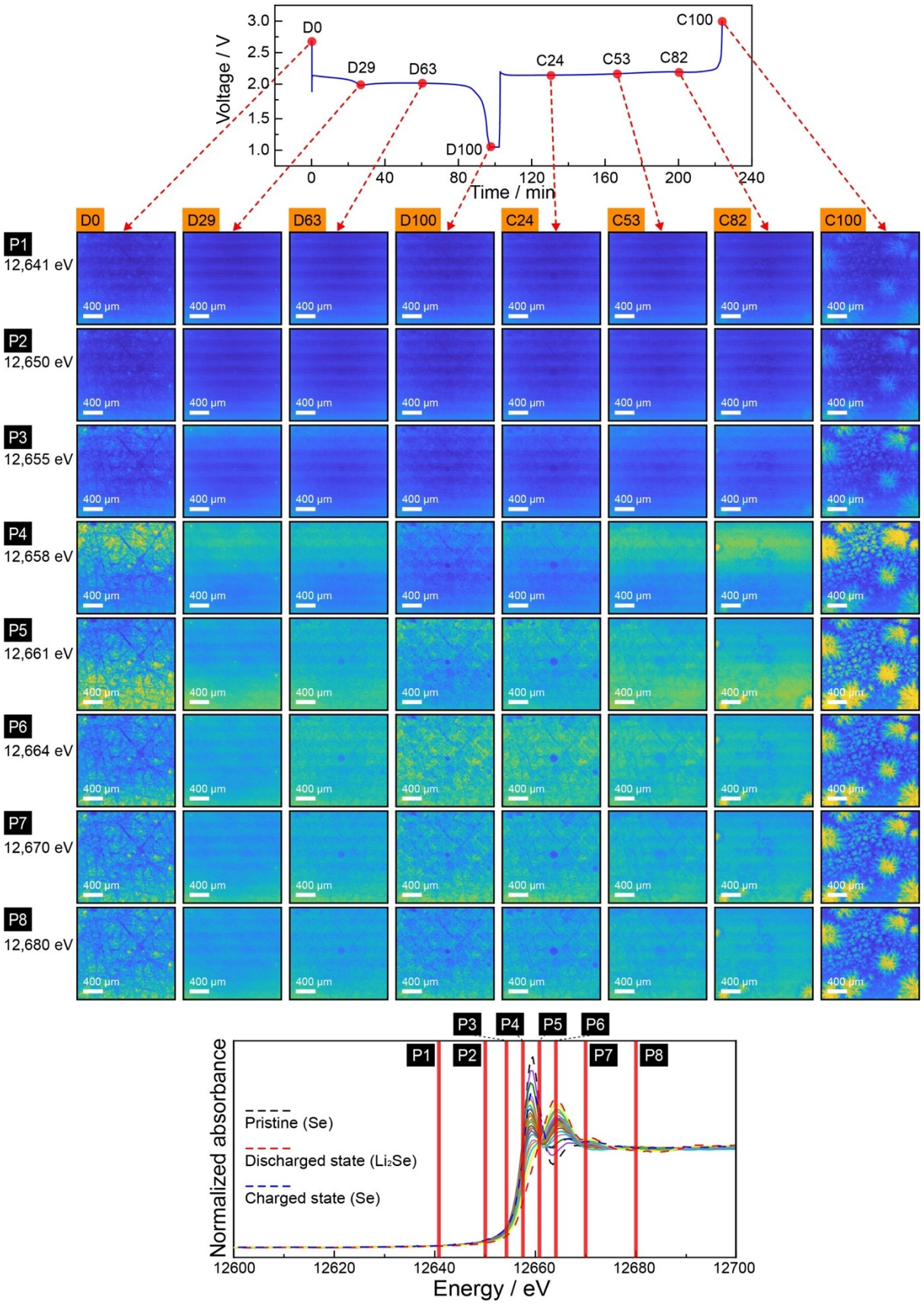

Fig. S4 *Operando* XANES images at the specific energies upon discharge and charge reactions.

Discussion for Fig. S4

The individual XANES images at a specific energy and a specific DOD or SOC are presented in Fig. S4. The image matrix of energy and DOD or SOC presents the progressive variations in the reduction of Se into Li_2Se (during the discharge) and the oxidation of Li_2Se into Se (during the charge), including the spatial chemical state distributions. As the photon energy changes, the intensity (brightness) of images changes, and the brightest moment is dependent on the phase in images. For example, for Se, the intensity is the highest at 12,658 eV, and for Li_2Se, it is at 12,664 eV, which can be confirmed in XANES spectra. For D0 and C100, the brightest images are observed at about 12,658 eV, whereas it is observed at about 12,664 eV for D100, indicating that Se is present in D0 and C100, whereas Li_2Se is present in D100. This is rough estimation, but through fitting process in each pixel based on reference spectra followed by reconstruction of mapping for each phase (e.g., Se, Li_2Se_n ($n \geq 4$), and Li_2Se), we can visualize the change of morphology and phase in real-time (see this result in Video S2).

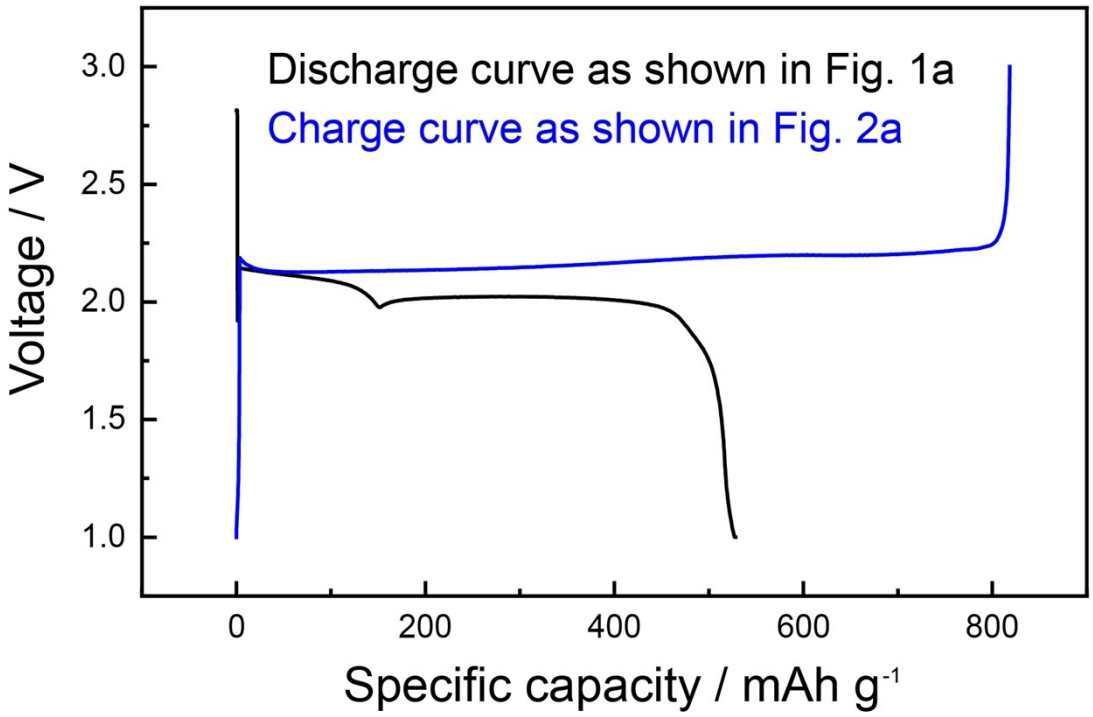

Fig. S5 Voltage profiles of a Se electrode in Figs. 1a and 2a as a function of specific capacity.

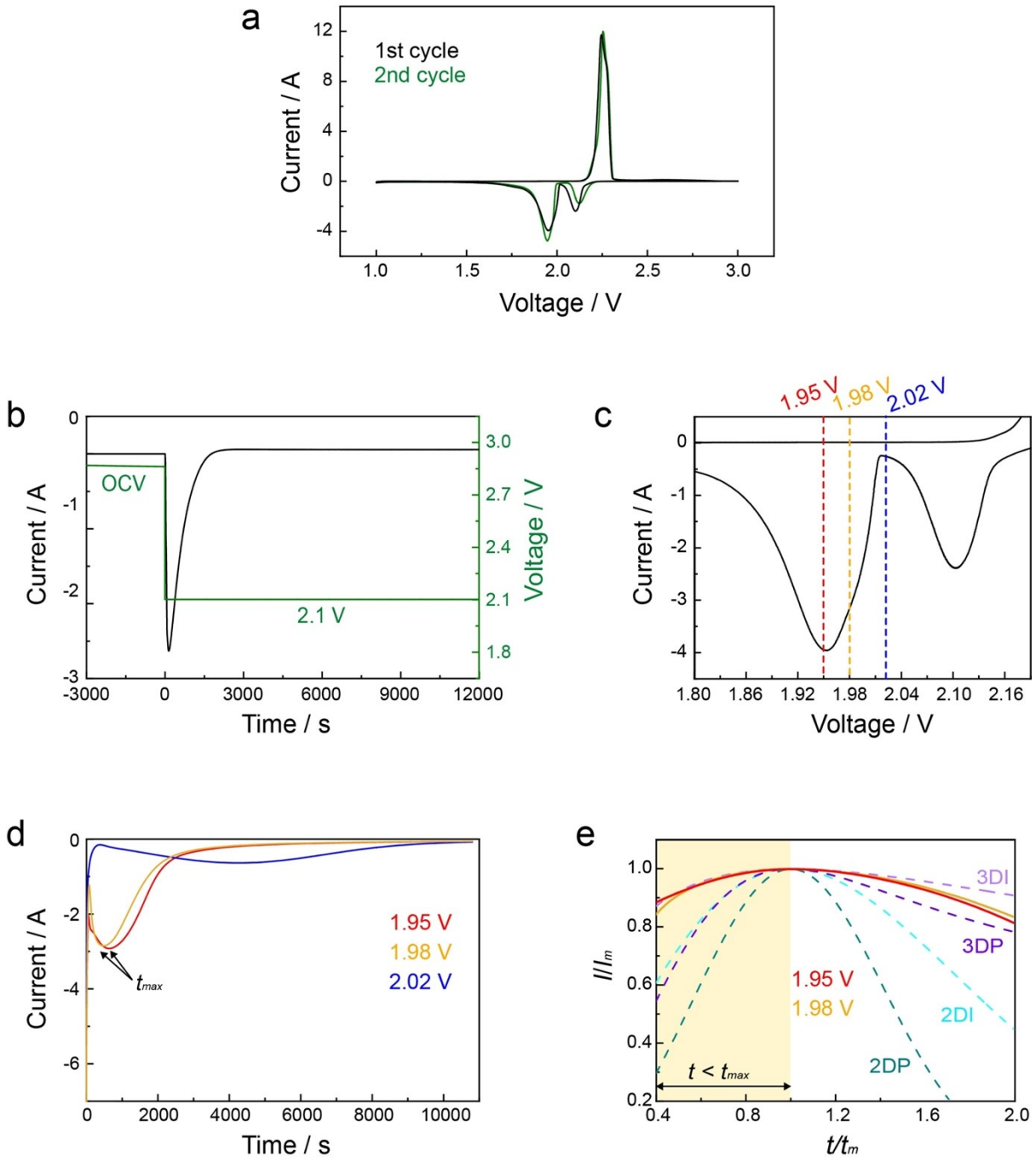

Fig. S6 (a) CV curves of Se cathode during two cycles. (b) Current response at the constant voltage of 2.1 V in CA. The OCV indicates an open-circuit voltage. (c) Enlarged the first CV curve of Fig. S6a. (d) Current responses at different voltages of 2.02 V, 1.98 V, and 1.95 V, following the reduction of polyselenides at 2.1 V. (e) Dimensionless current (I/I_m) and time (t/t_m) plots of theoretical models and experimental data at 1.98 V and 1.95 V.

Discussion for Fig. S6

As mentioned in Figs. 1g and 1h, the dimensionless current (I/I_m) and time (t/t_m) transients based on CA results are considered to fit four classical deposition models, wherein the way of nuclei formation is classified in progressive and instantaneous modes, and the direction of growth is classified in two-dimensional (2D) and three-dimensional (3D) modes. The 2D progressive (2DP) and 2D instantaneous (2DI) nucleation and growth modes follow the Bewick, Fleischmann, and Thirsk (BFT) models:[1]

$$\frac{I}{I_m} = \left(\frac{t}{t_m}\right)^2 exp\left[-\frac{2}{3}\left(\frac{t^3 - {t_m}^3}{{t_m}^3}\right)\right] \cdots S1\ for\ 2DP$$

$$\frac{I}{I_m} = \left(\frac{t}{t_m}\right) exp\left[-\frac{1}{2}\left(\frac{t^2 - {t_m}^2}{{t_m}^2}\right)\right] \cdots S2\ for\ 2DI$$

The 3D progressive (3DP) and 3D instantaneous (3DI) nucleation and growth modes follow the Scharifker and Hills (SH) models:[2]

$$\left(\frac{I}{I_m}\right)^2 = \frac{1.2254}{t/t_m}\left[1 - exp\left(-2.3367\frac{t^2}{{t_m}^2}\right)\right]^2 \cdots S3\ for\ 3DP$$

$$\left(\frac{I}{I_m}\right)^2 = \frac{1.9542}{t/t_m}\left[1 - exp\left(-1.2564\frac{t}{t_m}\right)\right]^2 \cdots S4\ for\ 3DI$$

To further confirm the reduction and oxidation reactions of Se electrode, a cyclic voltammetry (CV) was conducted in Fig. S6a. Upon discharge, distinct two reduction peaks at 2.1 V and 1.95 V of dissolving the Se and forming the Li_2Se are observed, consistent with the two voltage plateaus divided at 1.98 V in the voltage profile (Fig. 1a). Meanwhile, the oxidation of Li_2Se to Se_n^{2-} ($n \geq 4$) and final Se is observed as a single plateau (Fig. 2a) and a single oxidation peak (Fig. S6a) in multiple-phase transitions, which can be elucidated by a potential overlapping analogous to the S cathode.[3,4]

An exponentially decreasing behavior at the constant voltage of 2.1 V in CA curve (Fig. S6b) can identify the reduction of polyselenides prior to their deposition, since the reduction current of soluble polyselenides follows the exponentially decreasing curve in absence of the changes of electrode surface area such as deposition.[5] In enlarged CV curve (Fig. S6c), the second reduction peak of Li_2Se formation starts from ~2.02 V, and the peak reduction voltage is positioned at the 1.95 V. Accordingly, along with the CA curve at 2.0 V (Fig. 1g), the current response was further monitored at the constant voltages of 2.02 V, 1.98 V, and 1.95 V (Fig. S6d). It is note that the condition of 1.98 V is the inflection point in voltage profile (Fig. 1a). No significant initiation behavior of the nucleation is observed at 2.02 V, whereas the current responses at 1.98 V and 1.95 V represent the Li_2Se nucleation in exponentially increasing curve as well as the overlapping of neighboring nuclei at maximum current. The dimensionless

current (I/I_m) and time (t/t_m) transients at 1.98 V and 1.95 V (Fig. S6e) verify the 3DI nucleation and growth mode of Li_2Se before nuclei overlapping ($t < t_{max}$), wherein the experimental data are deviated from the 3DI theoretical model after nuclei overlapping. Therefore, along with the 3DI nucleation and growth mode at 2.0 V (Figs. 1g and 1h), it can be delivered that the nucleation of Li_2Se starts between 2.02 V and 2.0 V, and the nucleation and growth behavior on Li_2Se follows the 3DI mode at least until the nuclei overlapping.

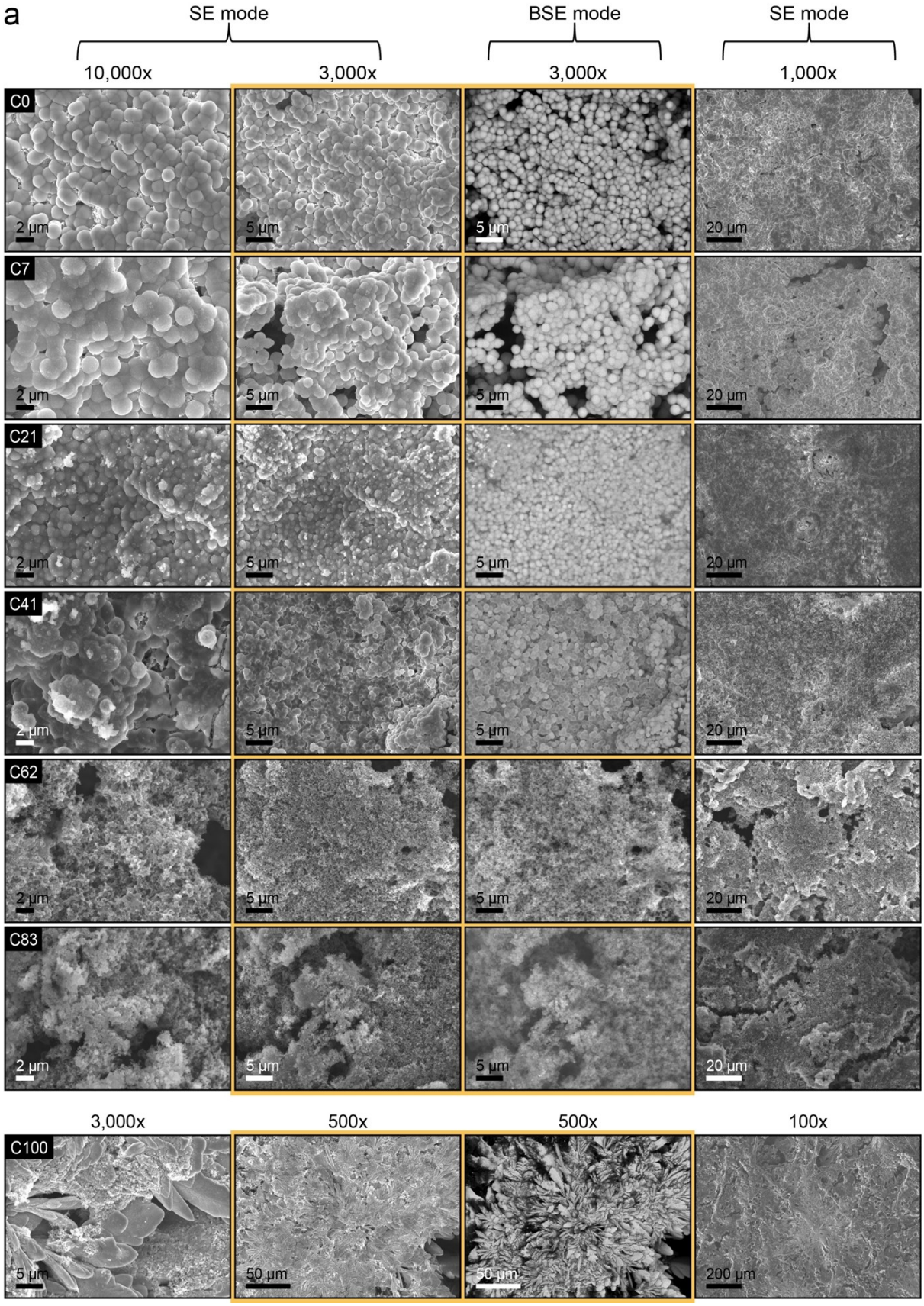
a
SE mode
BSE mode
SE mode
10,000x
3,000x
3,000x
1,000x
C0
C7
C21
C41
C62
C83
C100
2 μm
5 μm
20 μm
3,000x
500x
500x
100x
50 μm
200 μm

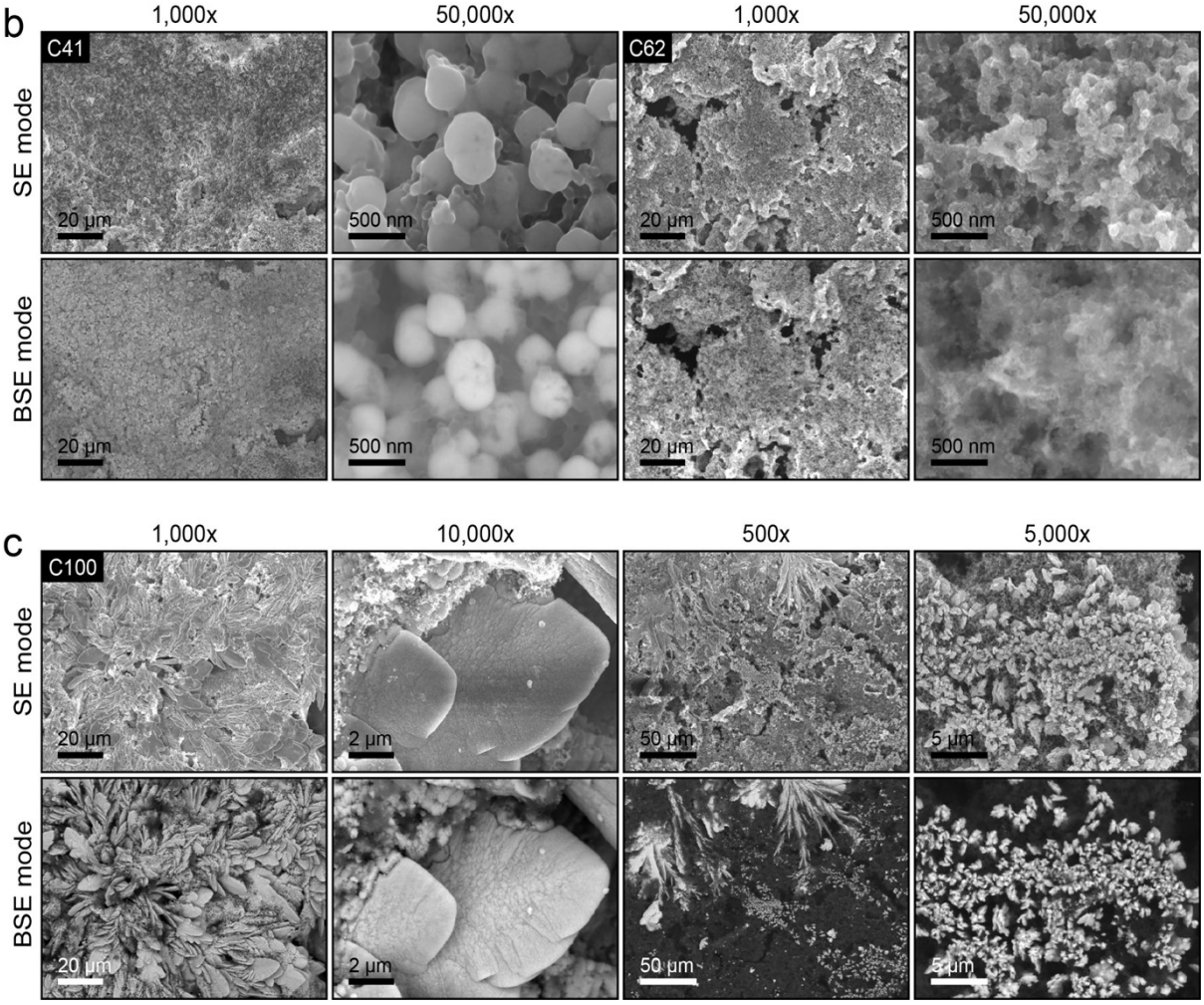

Fig. S7 (a) *Ex-situ* SEM images at the specific SOCs in SE and BSE modes with the same magnification as indicated by yellow box. (b) SEM images of Se electrode at C41 and C62 in SE and BSE modes. The dissolving Li_2Se until C62 is confirmed by BSE-SEM. (c) SEM images of Se electrode in SE and BSE modes at C100.

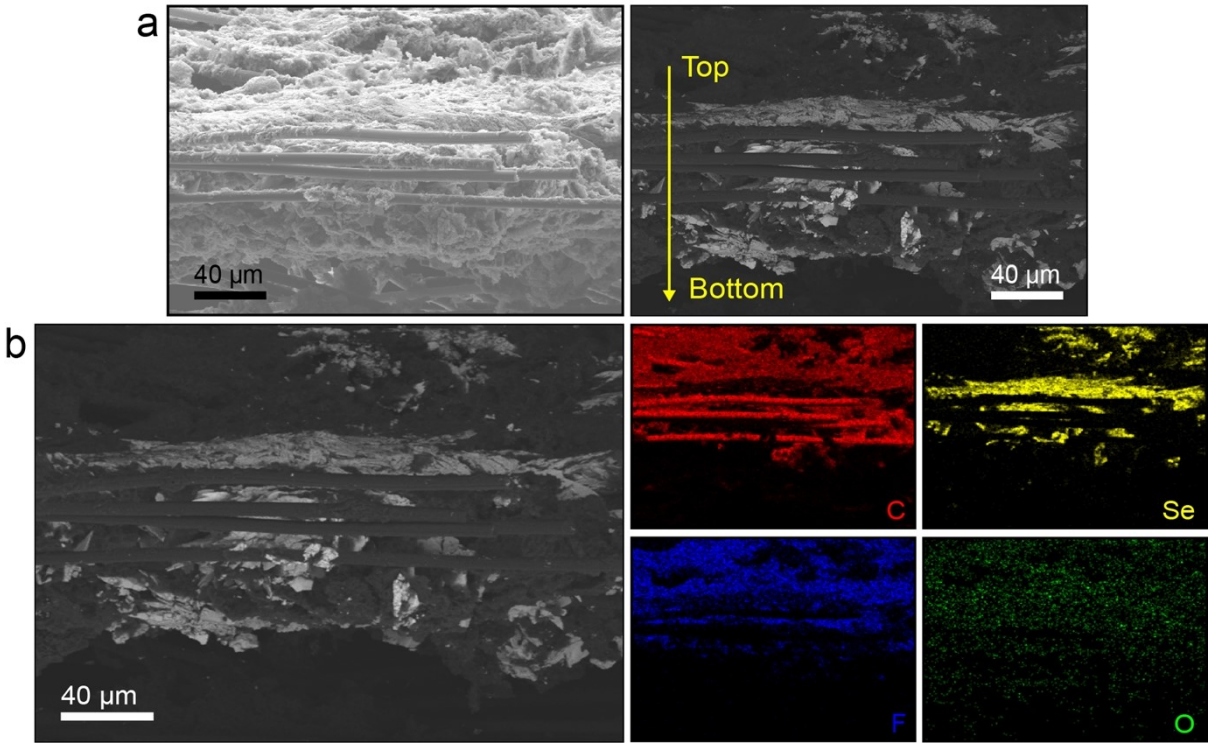

Fig. S8 (a) Cross-sectional SEM images of Se electrode at C100 in SE (left) and BSE (right) modes. (b) EDX mapping of cross-sectional Se electrode at C100.

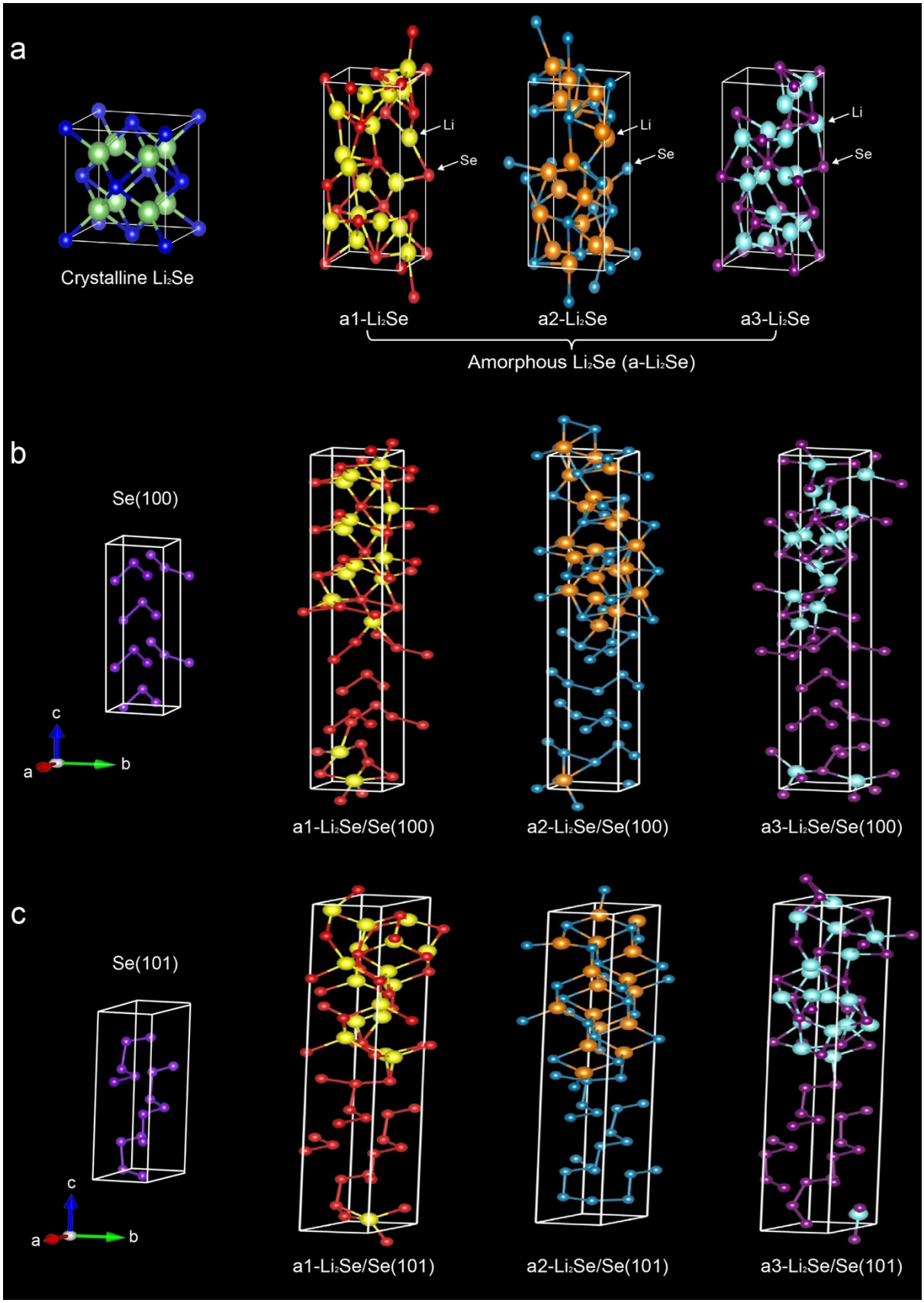
a
Crystalline Li₂Se
Li
Se
a1-Li₂Se
a2-Li₂Se
a3-Li₂Se
Amorphous Li₂Se (a-Li₂Se)
b
Se(100)
c
a
b
a1-Li₂Se/Se(100)
a2-Li₂Se/Se(100)
a3-Li₂Se/Se(100)
c
Se(101)
c
a
b
a1-Li₂Se/Se(101)
a2-Li₂Se/Se(101)
a3-Li₂Se/Se(101)

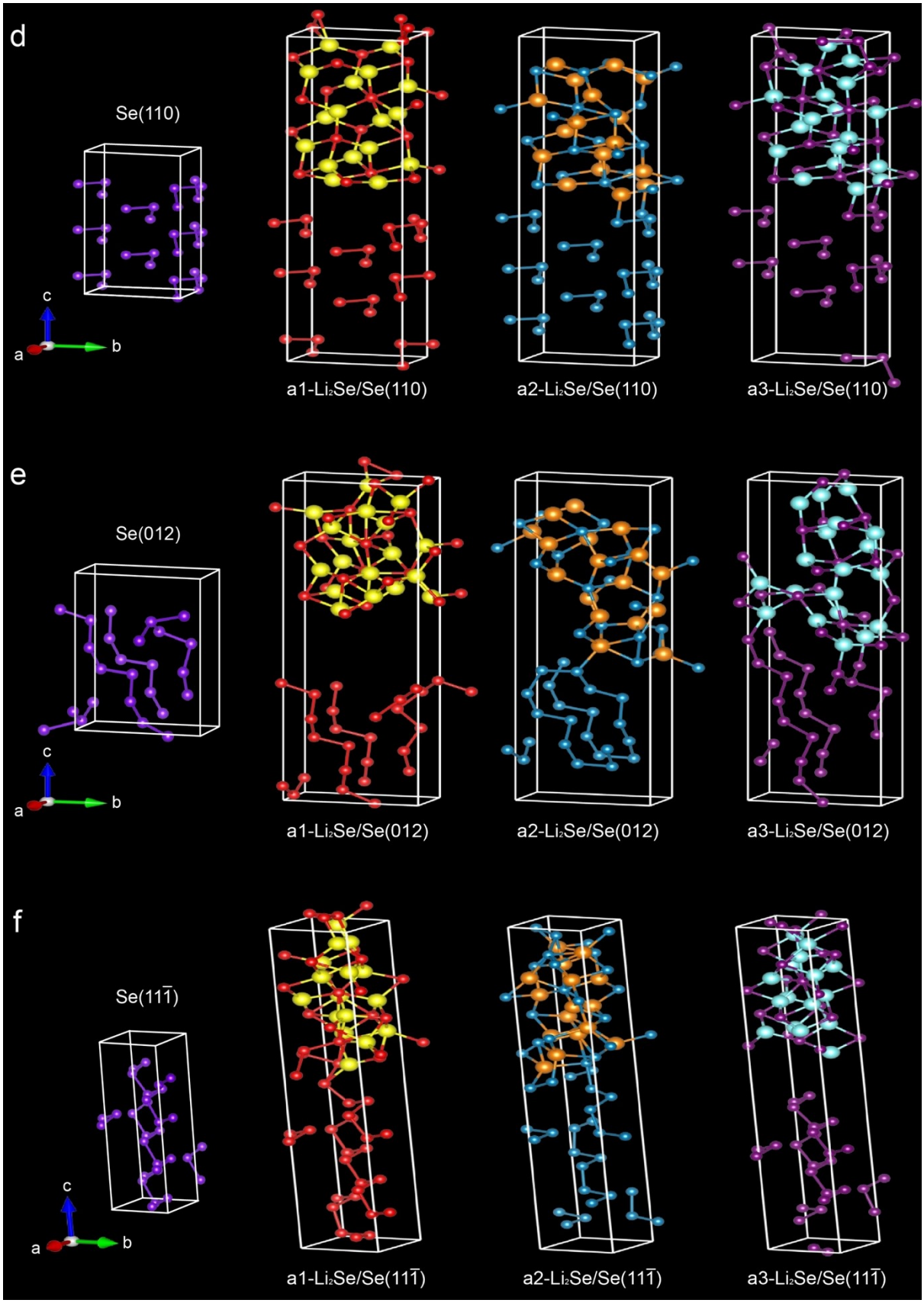
d
Se(110)
c
a
b
a1-Li₂Se/Se(110)
a2-Li₂Se/Se(110)
a3-Li₂Se/Se(110)
e
Se(012)
c
a
b
a1-Li₂Se/Se(012)
a2-Li₂Se/Se(012)
a3-Li₂Se/Se(012)
f
Se(11$\bar{1}$)
c
a
b
a1-Li₂Se/Se(11$\bar{1}$)
a2-Li₂Se/Se(11$\bar{1}$)
a3-Li₂Se/Se(11$\bar{1}$)

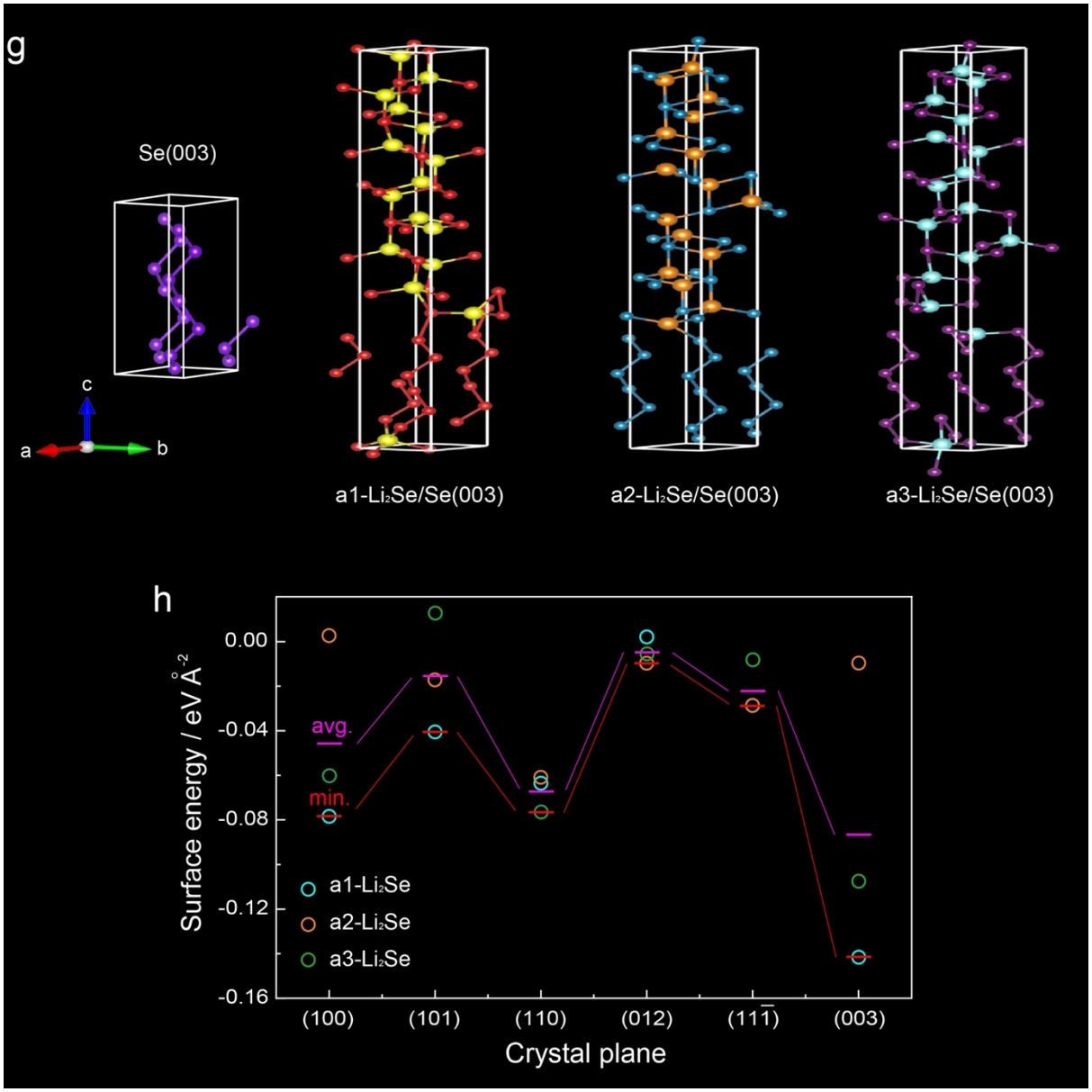

Fig. S9 (a) Crystalline Li_2Se structure and three different amorphous Li_2Se structures designed in our work as indicated by a1-Li_2Se, a2-Li_2Se, and a3-Li_2Se. (b)-(g) DFT modeling on six crystal planes of hexagonal Se in contact with the amorphous Li_2Se phases. (h) Surface energy of each crystal plane in contact with three different amorphous Li_2Se interfaces. The "avg." means an average surface energy at the a1-Li_2Se, a2-Li_2Se, and a3-Li_2Se interfaces. The "min." means a minimum surface energy among the a1-Li_2Se, a2-Li_2Se, and a3-Li_2Se interfaces at each crystal plane.

Table S1 DFT data collection for the surface energy of each Se crystal plane in contact with three different amorphous Li_2Se interfaces

		Total free energy of Se/ Li_2Se interface / eV	Free energy of Se / eV	Free energy of Li_2Se / eV	Area / Å^2	Surface energy / eV Å^{-2}
(100)	a1-Li_2Se	-126.6449	-41.8953	-81.1713	22.8235	-0.0784
	a2-Li_2Se	-126.9099	-41.8994	-85.1274	22.8235	0.0026
	a3-Li_2Se	-124.5201	-41.8764	-79.8896	22.8235	-0.0603
	avg.	-126.0250	-41.8903	-82.0628	22.8235	-0.0454
(101)	a1-Li_2Se	-130.3050	-44.2586	-83.7050	28.8758	-0.0405
	a2-Li_2Se	-130.6361	-44.5392	-85.0987	28.8758	-0.0173
	a3-Li_2Se	-129.0585	-44.5596	-85.2271	28.8758	0.0126
	avg.	-129.9999	-44.4525	-84.6770	28.8758	-0.0151
(110)	a1-Li_2Se	-137.0202	-55.2404	-76.7563	39.5309	-0.0635
	a2-Li_2Se	-137.0070	-55.3277	-76.8587	39.5309	-0.0610
	a3-Li_2Se	-137.0298	-54.0537	-76.9231	39.5309	-0.0766
	avg.	-137.0190	-54.8739	-76.8460	39.5309	-0.0670
(012)	a1-Li_2Se	-135.8036	-84.9439	-51.0348	42.1014	0.0021
	a2-Li_2Se	-135.5798	-50.6262	-84.1298	42.1014	-0.0098
	a3-Li_2Se	-135.1469	-49.9821	-84.6887	42.1014	-0.0057
	avg.	-135.5101	-61.8508	-73.2844	42.1014	-0.0045
$(11\bar{1})$	a1-Li_2Se	-158.2053	-71.7520	-83.9661	43.3081	-0.0287
	a2-Li_2Se	-158.2226	-71.7736	-83.9639	43.3081	-0.0287
	a3-Li_2Se	-156.6281	-71.8988	-84.0105	43.3081	-0.0083
	avg.	-157.6853	-71.8081	-83.9802	43.3081	-0.0219
(003)	a1-Li_2Se	-110.4480	-23.2785	-82.1608	17.6893	-0.1416
	a2-Li_2Se	-110.5743	-23.5512	-86.6789	17.6893	-0.0097
	a3-Li_2Se	-110.9657	-23.4140	-83.7442	17.6893	-0.1076
	avg.	-110.6627	-23.4146	-84.1946	17.6893	-0.0863

Discussion for Fig. S9

To further confirm the preferred growth of $[001]$ for charged Se, we conducted the DFT calculations as follows. As an alternative to the electrolyte-soluble polyselenides, amorphous Li_2Se was designed in the simulations. Amorphous structure is pure random structure. To represent the non-crystallinity of random structures, different structures with local structural disordering were generated from high temperature melting and rapidly quenching simulations by *ab initio* molecular dynamics. Then, the surface energy of each Se crystal plane in contact with the amorphous Li_2Se was calculated in Fig. S9 and Table S1. Since the energy value in amorphous phase greatly varies depending on the atomic structure, three different structures of amorphous Li_2Se were employed in the DFT calculations (Fig. S9a). The six crystal planes of hexagonal $P3_121$ structure in order of low index and high XRD peak intensity, (100), (101), (110), (012), $(11\bar{1})$, and (003), were confirmed in the calculations. The absence of (201) plane corresponding to $(20\bar{2}1)$ was attributed to the structure similarity with the (101) plane of $(10\bar{1}1)$. Based on the DFT modeling results (Figs. S9b-g and Table S1), Fig. S9h presents the significantly similar trend in surface energies on the six interfaces, at both the average and the minimum values. In contrast to the high surface energy of a2, the surface energies of a1 and a3 at the (003) plane are particularly lower than the a1, a2, and a3 values of all planes. The remarkably low surface energies of a1 and a3 at the (003) can imply that there are few opportunities to adsorb on not only the other five planes but also the (003) plane of a2. Accordingly, it can be supported that the thermodynamically stable plane of (003) contributes to the favored deposition and growth along the $[001]$ direction.[6-8]

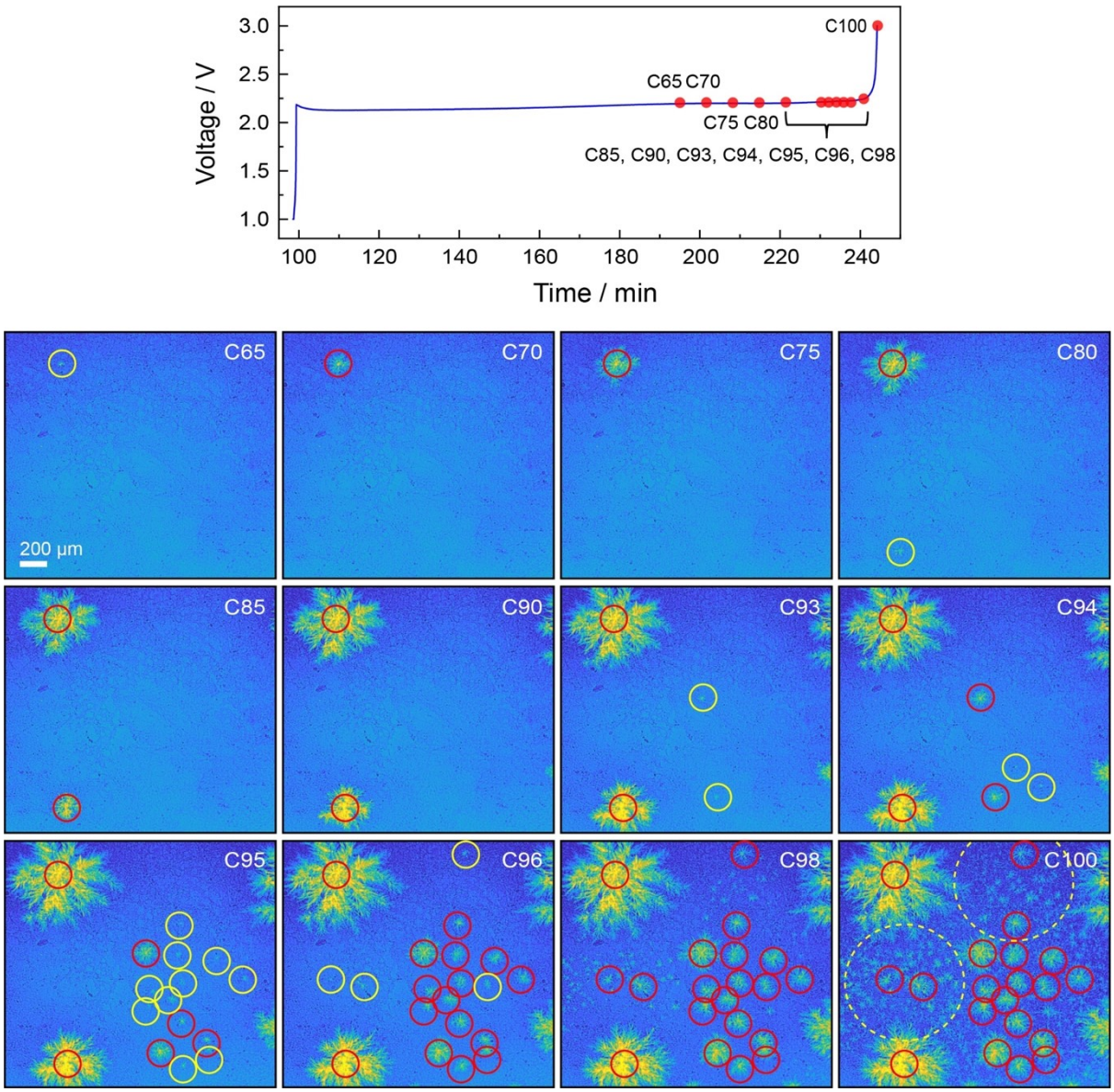

Fig. S10 Charge voltage profile of the Se electrode at 0.5 C for the first cycle and TXM images within specifically divided timelines for confirming the simultaneous advent of nuclei and their growth period. Noteworthy, at C96, there is a difference between the notation in yellow and red circles of Fig. S10 and Fig. 3a by the tracking in a continuous image array. The yellow dotted circles at C100 indicate the depletion of polyselenides by selectively grown large Se.

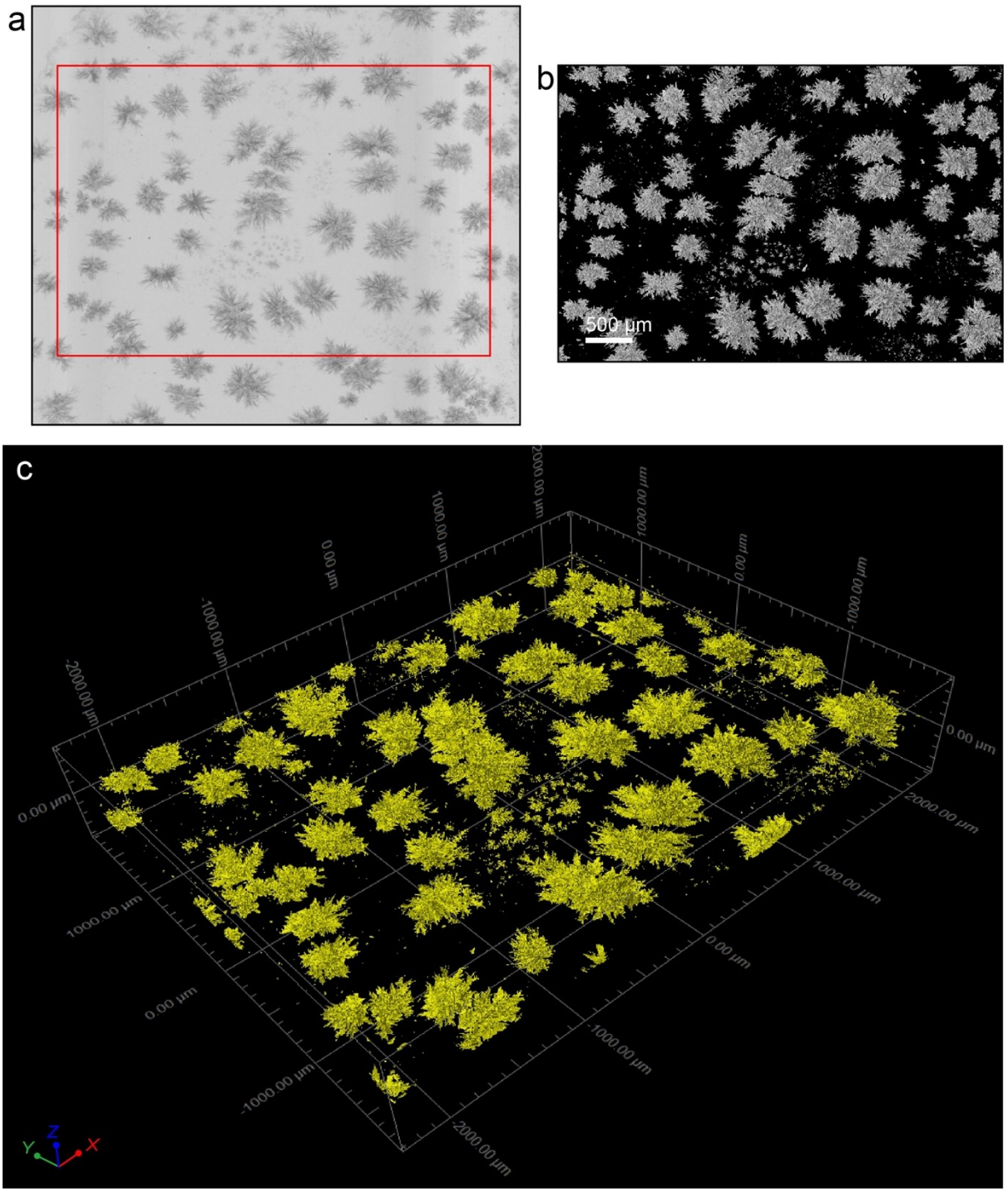
a
b
500 µm
c
2000.00 µm
1000.00 µm
0.00 µm
-1000.00 µm
-2000.00 µm
Z
Y
X

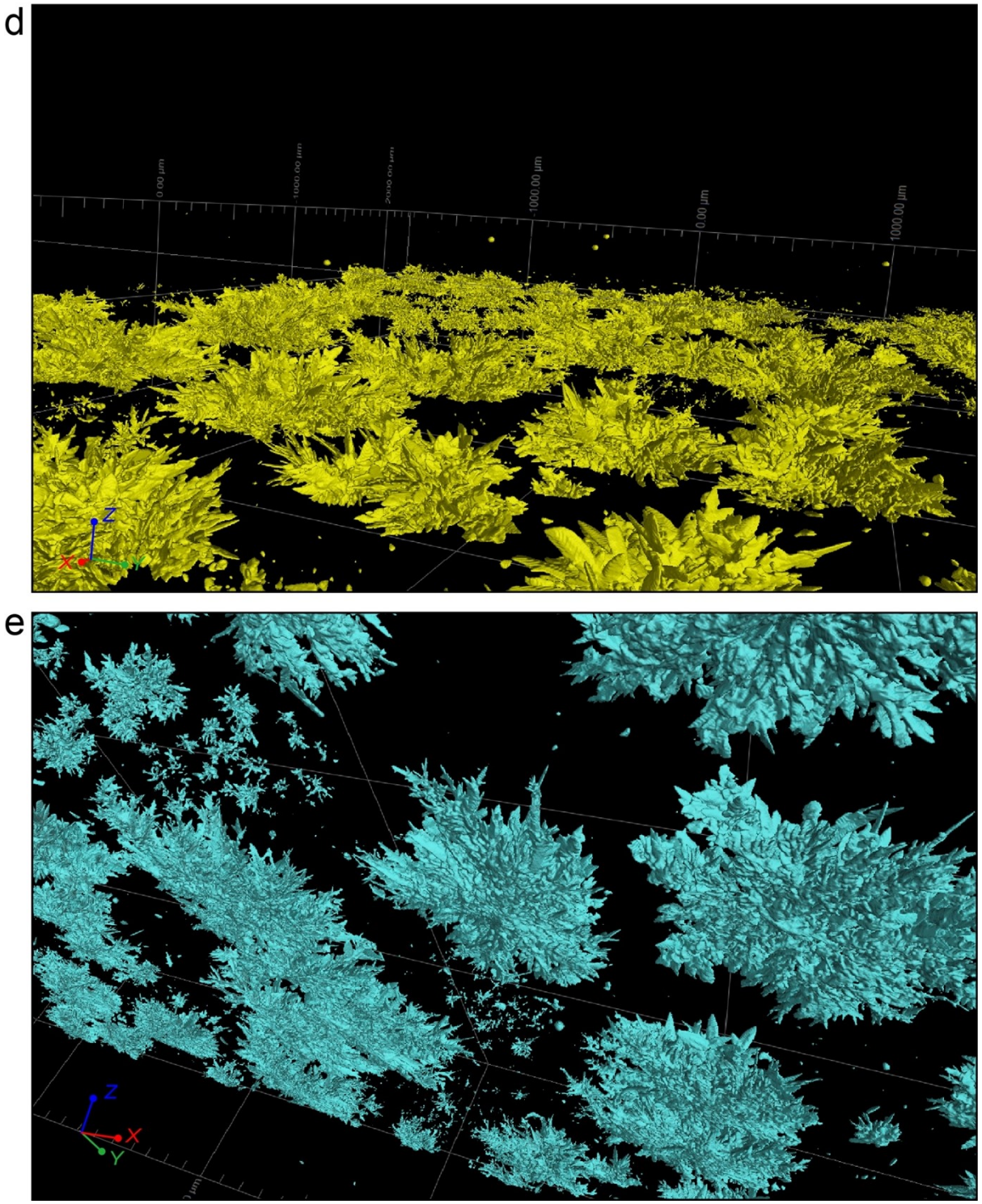

Fig. S11 (a) Full X-ray image of the charged Se electrode. (b) CT image corresponding to red box in Fig. S11a. (c) CT image of Fig. S11b at the different directions. CT images (d) from the top looking down direction and (e) from the bottom looking up direction.

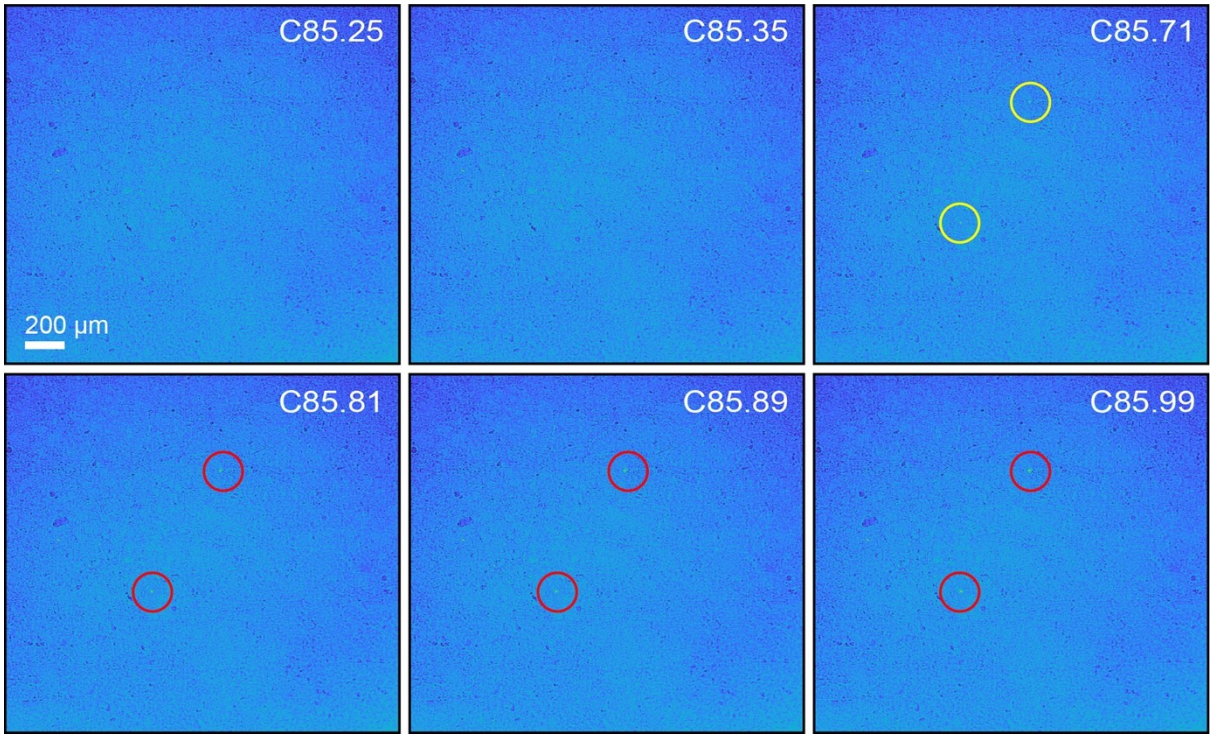

Fig. S12 TXM images within specifically divided timelines for confirming the simultaneous formation of two nuclei.

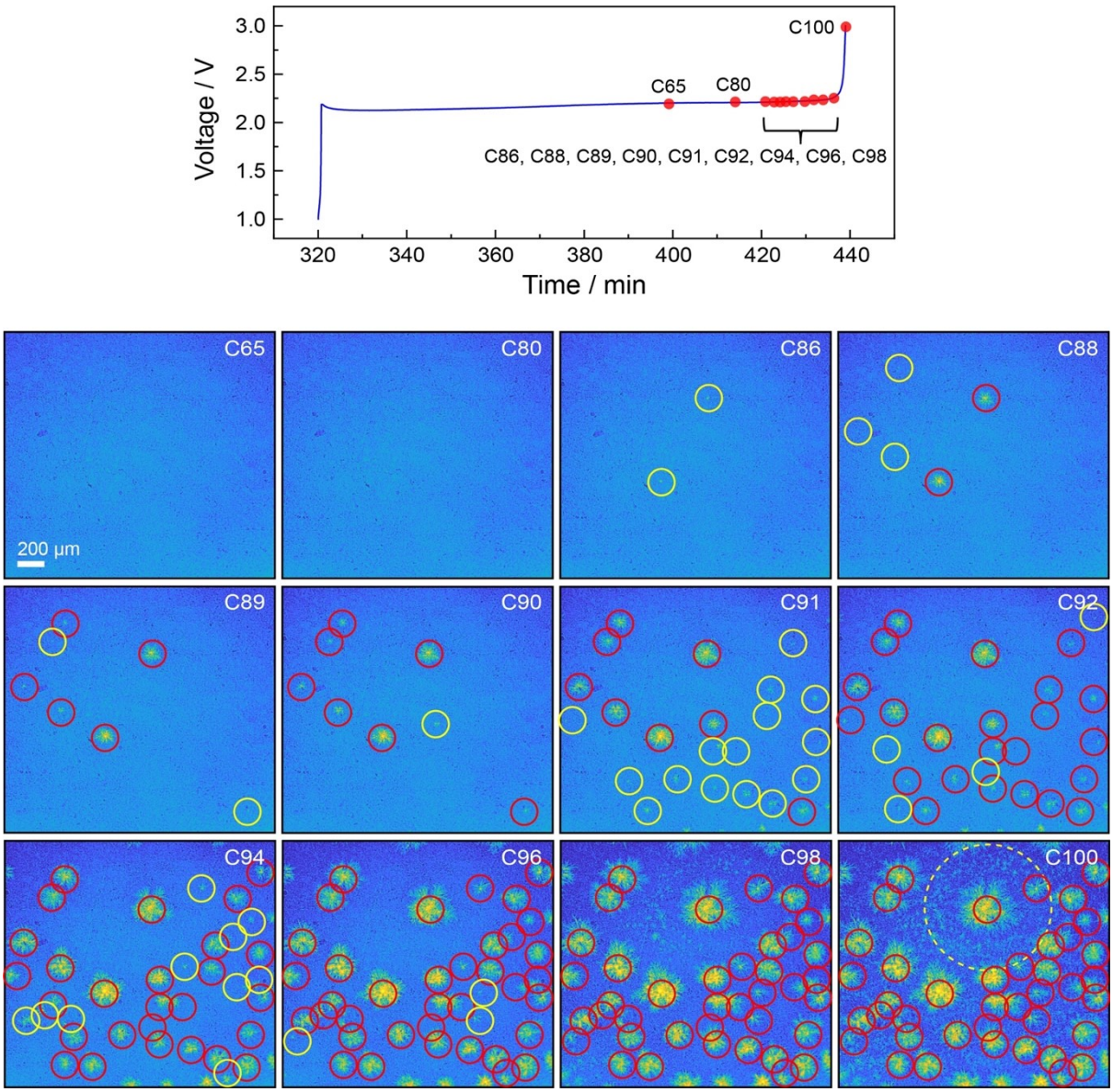

Fig. S13 Charge voltage profile of the Se electrode at 0.5 C for the second cycle and TXM images within specifically divided timelines for confirming the simultaneous advent of nuclei and their growth period. The yellow dotted circle at C100 indicates the depletion of polyselenides by selectively grown large Se.

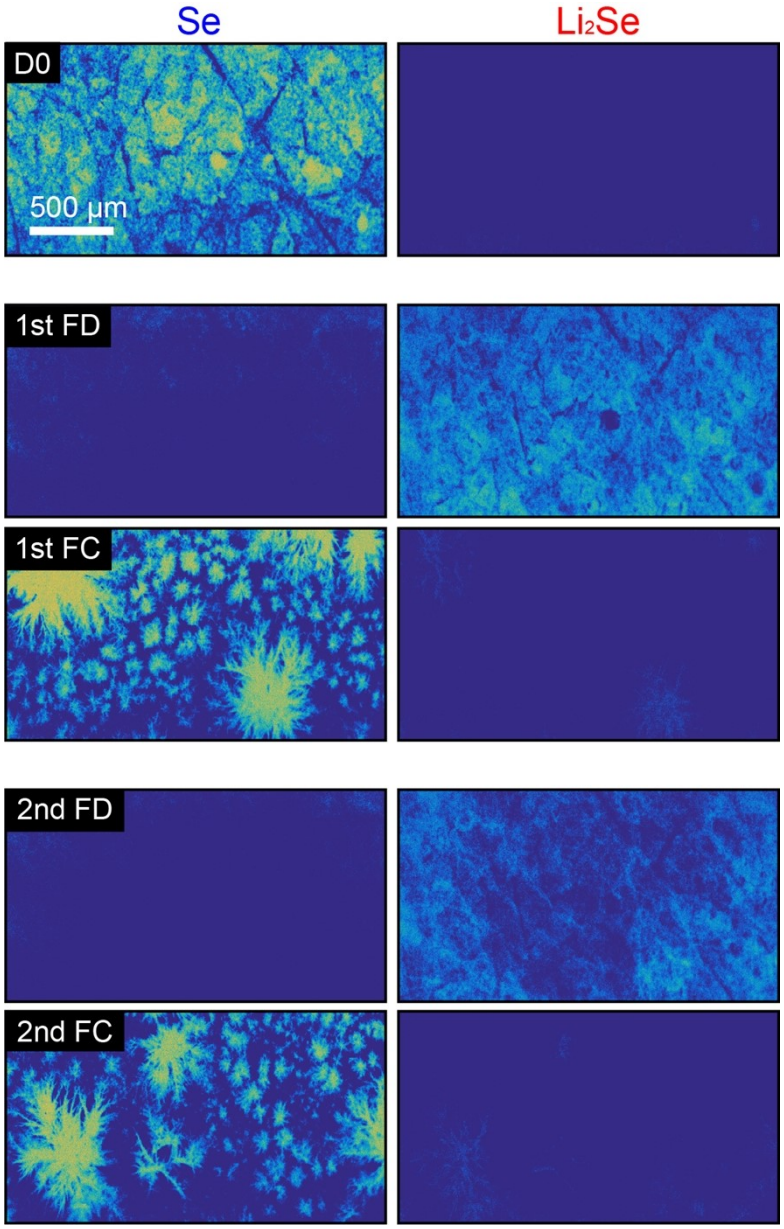

Fig. S14 Chemical state mappings of Se and Li_2Se phases by *operando* XANES imaging during two cycles.

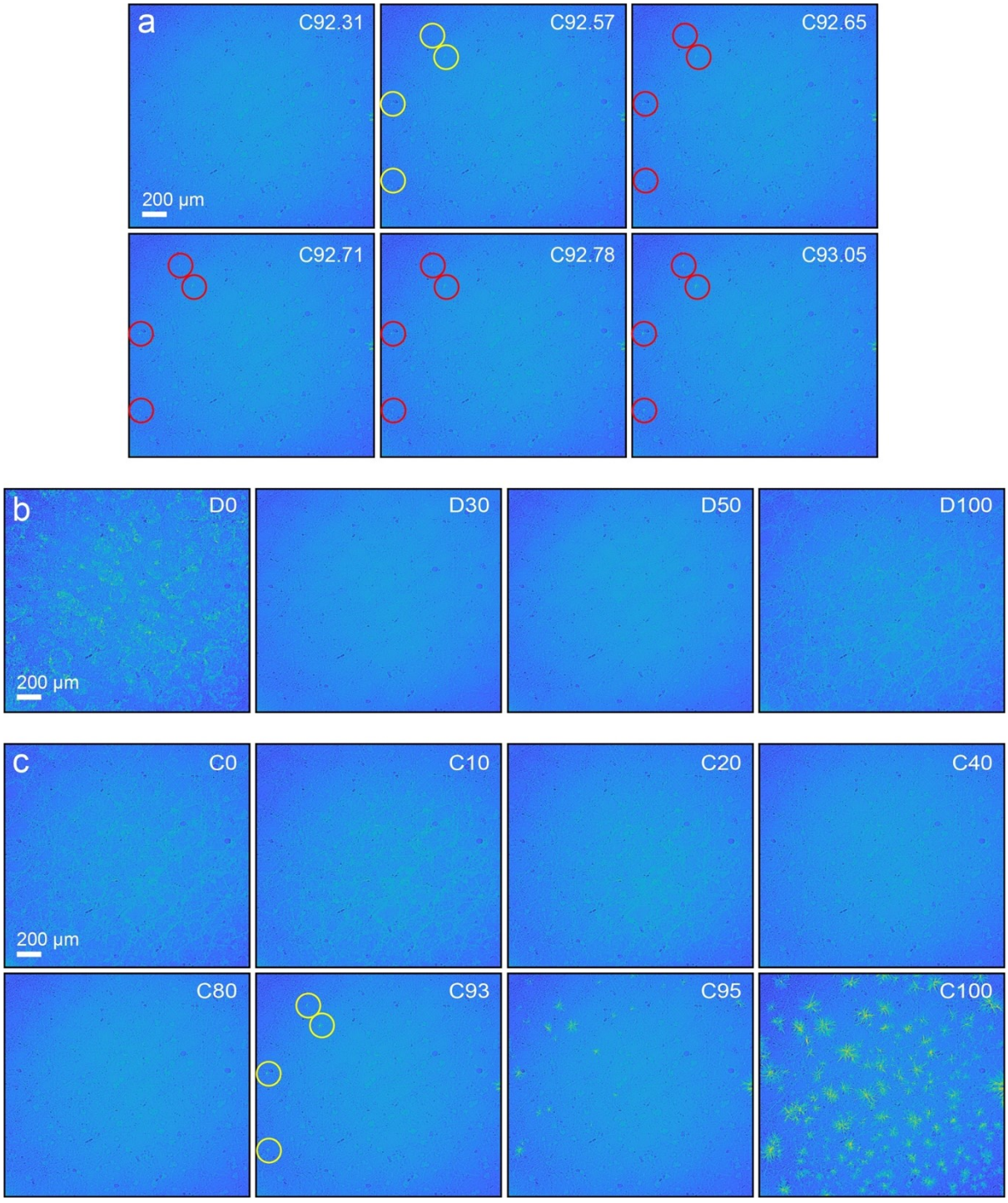

Fig. S15 (a) TXM images of the electrode with Se loading of ~1 mg cm^{-2} within specifically divided timelines for confirming the simultaneous formation of four nuclei. TXM images of the electrode with ~1 mg cm^{-2} Se loading during (b) discharge and (c) charge.

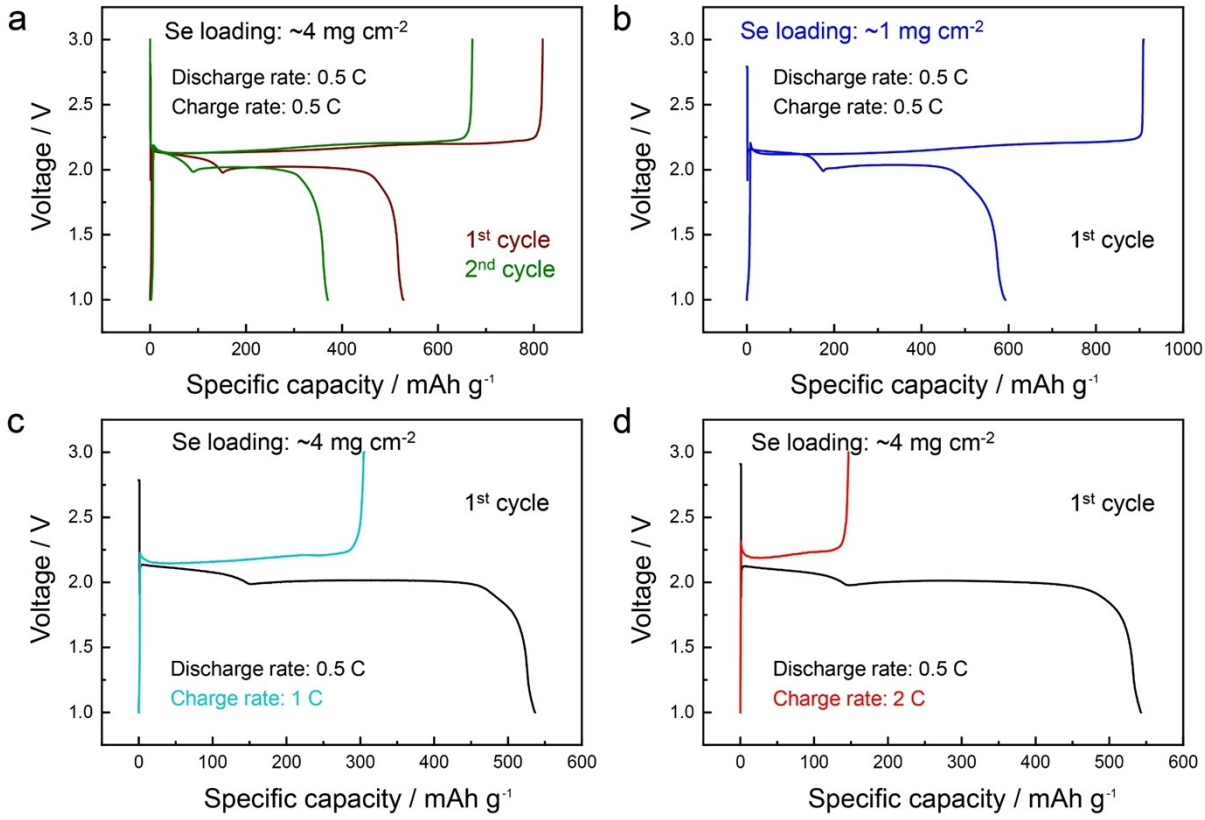

Fig. S16 Voltage profiles of a Se electrode in (a) Fig. 4a, (b) Fig. 4b, and (c, d) Fig. 4c as a function of specific capacity.

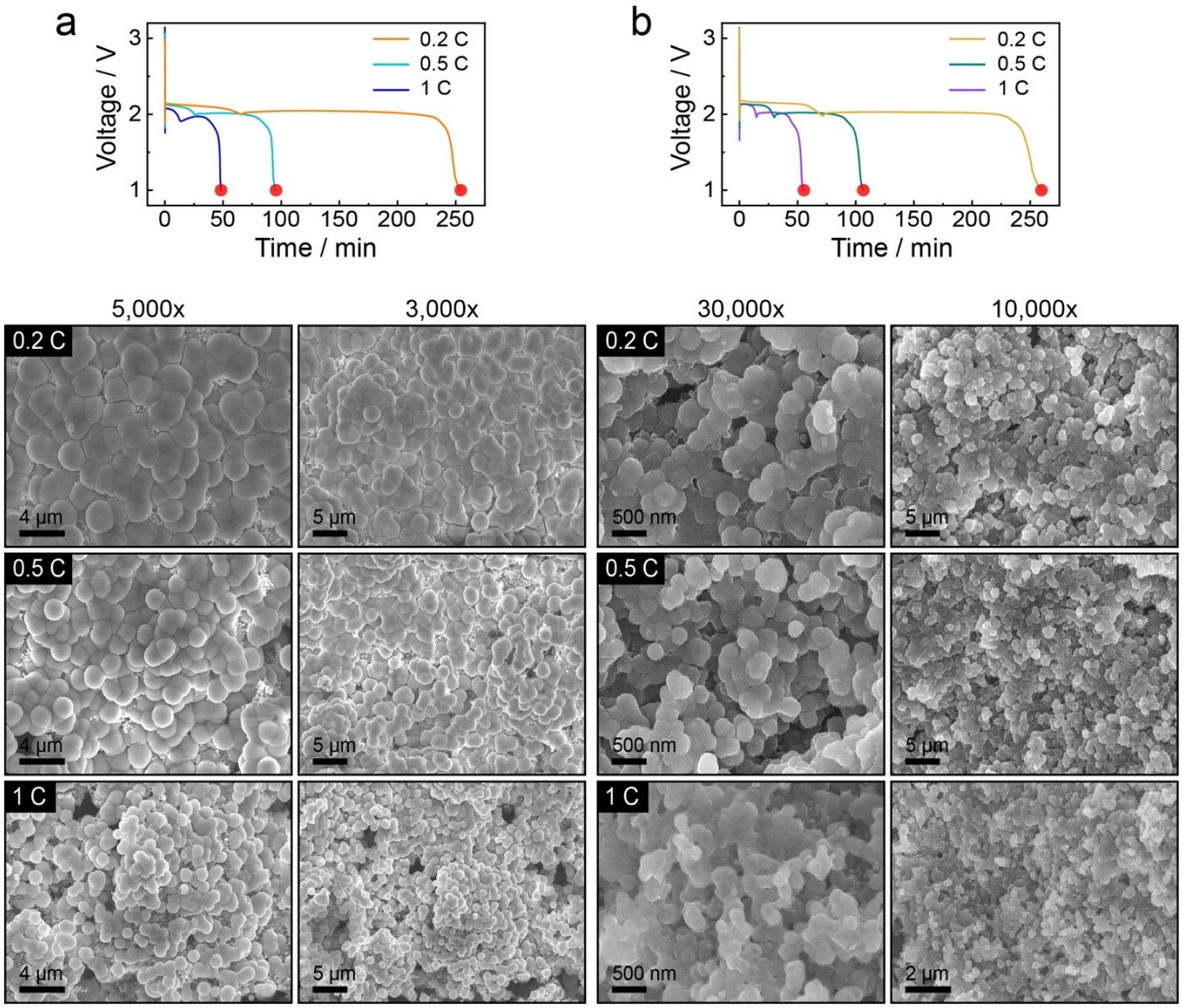

Fig. S17 Discharge voltage profiles for the first cycle and *ex-situ* SEM images of the electrodes with different Se loading of (a) ~4 mg cm^{-2} and (b) ~1 mg cm^{-2} at various current rates of 0.2 C, 0.5 C, and 1 C. The red circle in each voltage profile indicates the state of D100.

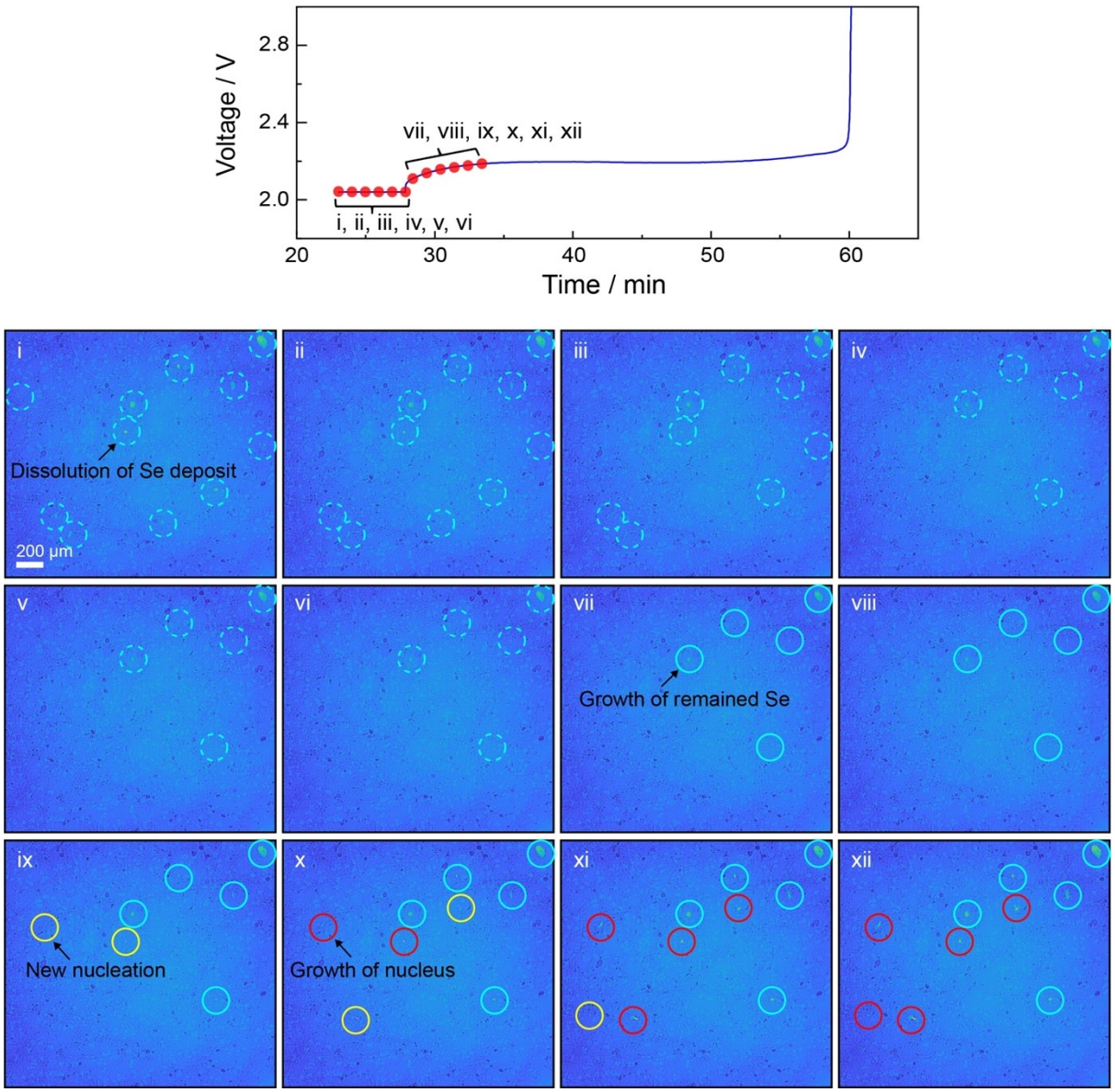

Fig. S18 Voltage profile of the Se electrode at 0.5 C during a holding the potential for 5 min at 2.04 V and subsequent charge processes, and TXM images for confirming the dissolution of Se deposits during the potential holding at 2.04 V (i, ii, iii, iv, v, and vi) and the growth of remained Se during the charge (vii, viii, ix, x, xi, and xii).

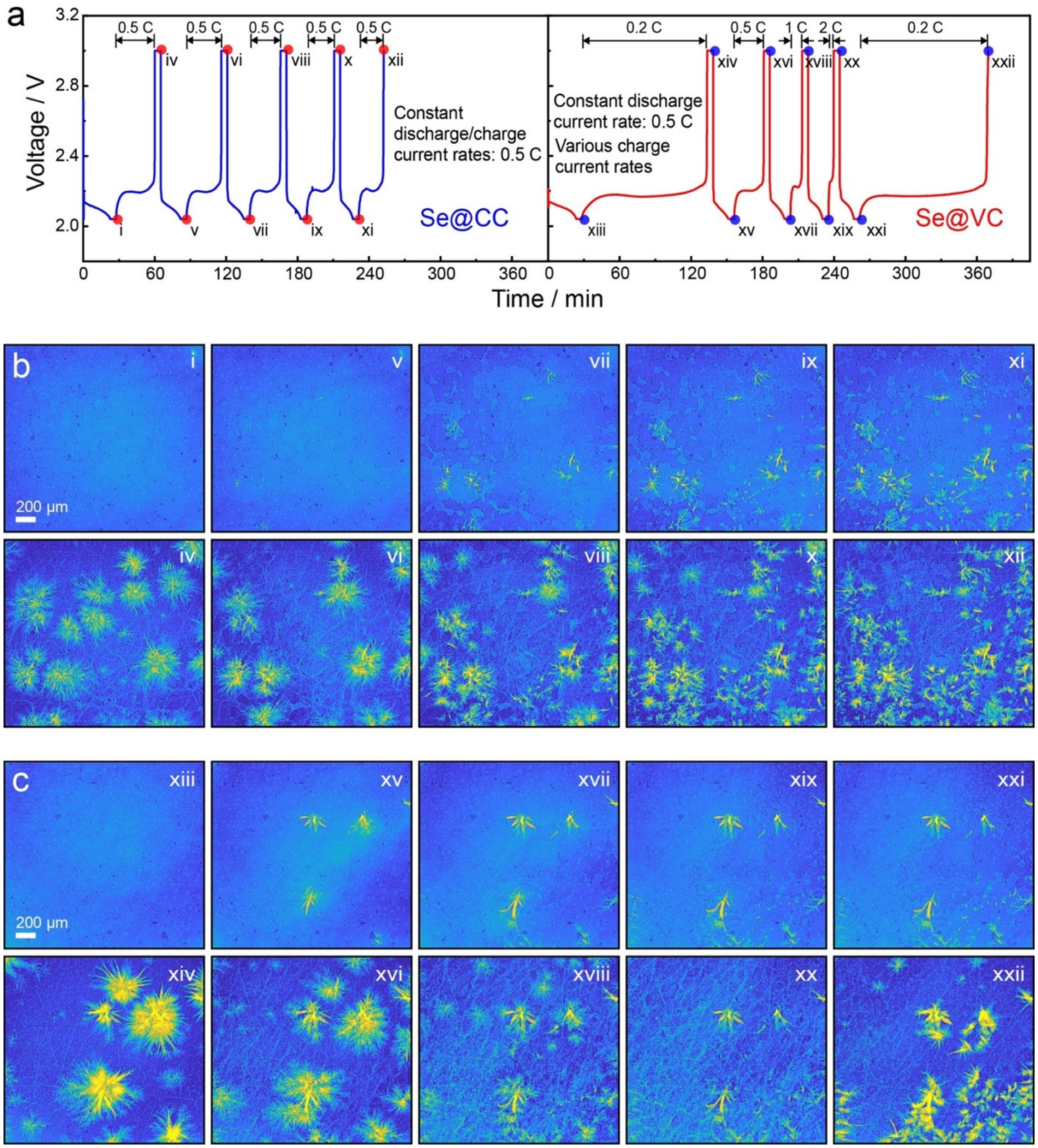

Fig. S19 (a) Voltage profiles of Se@CC and Se@VC electrodes for 5 cycles. TXM images of (b) Se@CC and (c) Se@VC electrodes at each discharged and charged states. The red and blue circles indicate the discharged and charged states after the potential holding for 5 min at 2.04 V, wherein the last ones of xii and xxii correspond to the end of the 5th charge before holding.

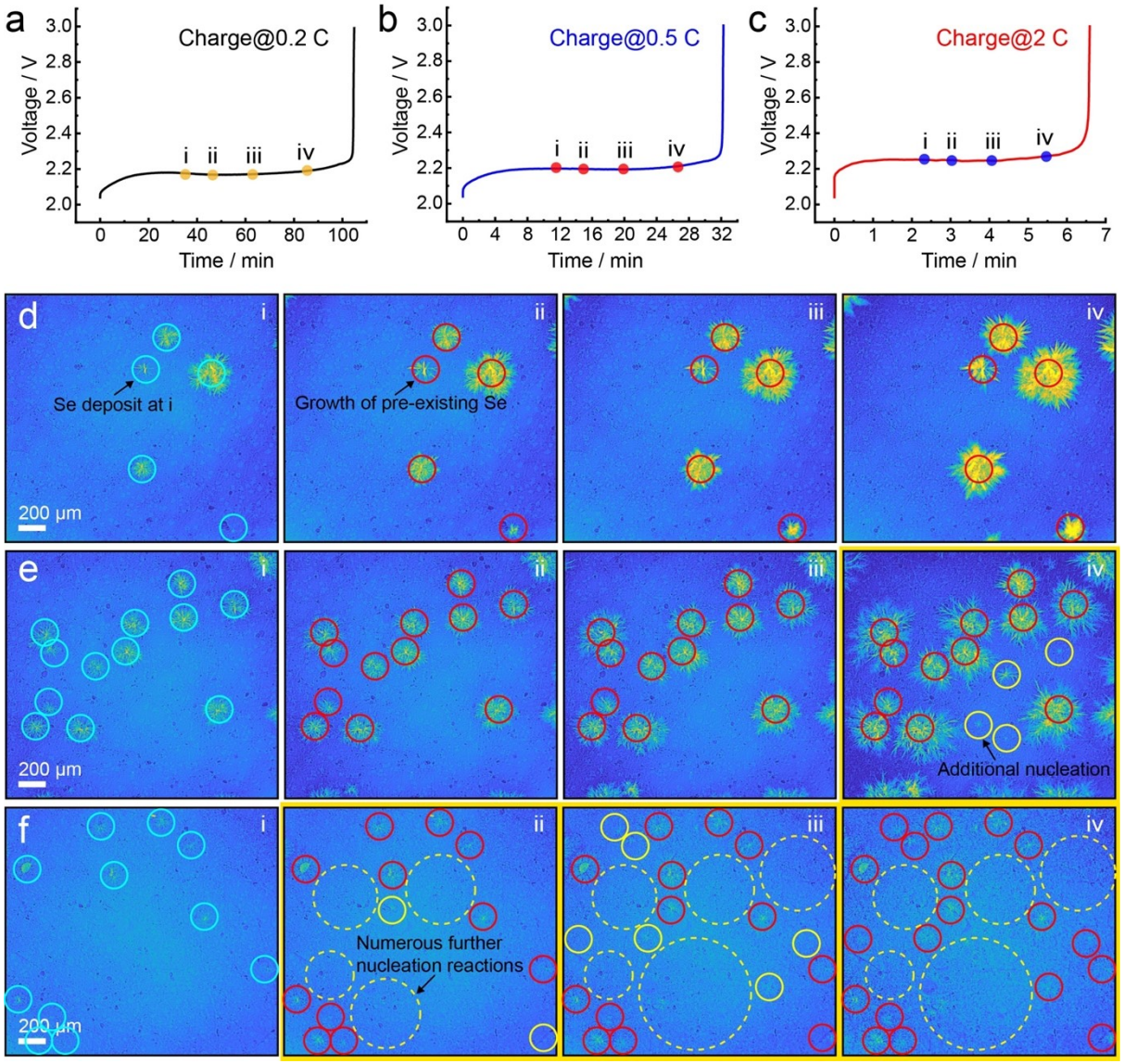

Fig. S20 Charge voltage profiles of the electrodes at different charge current rates of (a) 0.2 C, (b) 0.5 C, and (c) 2 C. The indications of i, ii, iii, and iv correspond to 36, 46, 61, and 83% SOC, respectively. TXM images at i, ii, iii, and iv of the electrodes at (d) 0.2 C, (e) 0.5 C, and (f) 2 C. Compared to the growth of pre-existing Se at charge current rate of 0.2 C (Fig. S20d), the further nucleation at higher current rates of 0.5 C (Fig. S20e) and 2 C (Fig. S20f) is highlighted by yellow boxes.

Discussion for Fig. S20

In addition to the first charge current rates of 0.5 C (Se@CC) and 0.2 C (Se@VC), the high current rate of 2 C was further applied during charge (Video S8 and Fig. S20c). All the three electrodes have the first discharge at 0.5 C. Depending on the charge current rate, the different nucleation/growth behaviors are observed. At the low current rate of 0.2 C (Fig. S20a), only growth is observed until iv, but at the high current rate of 2 C, both growth of pre-existing Se and additional nucleation occur simultaneously (Fig. S20c). It is worth noting that at higher current density, the additional nucleation appears earlier (at ii at 2 C rate *vs.* at iv at 1 C rate).

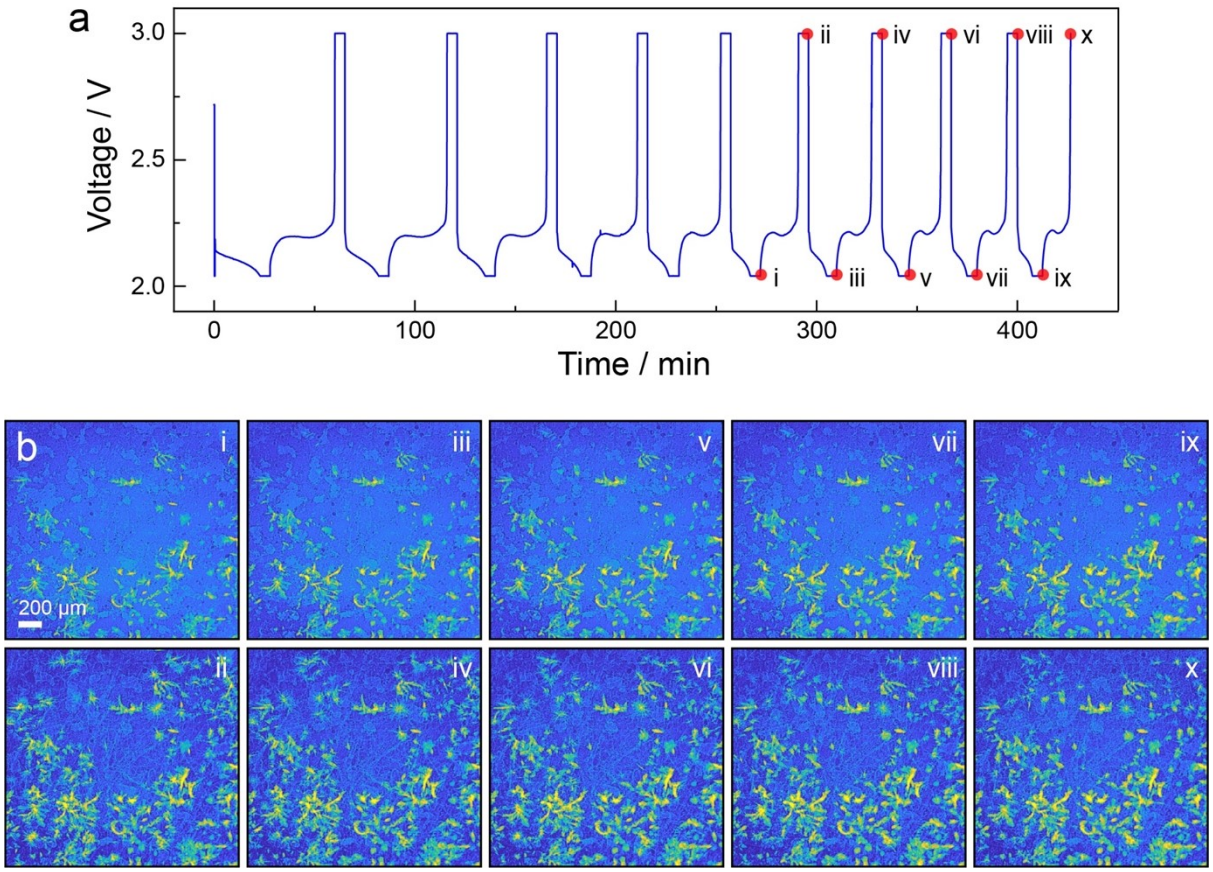

Fig. S21 (a) Voltage profiles Se@CC electrode at 0.5 C for 10 cycles. (b) TXM images of Se@CC at each discharged and charged states after the potential holding for 5 min, wherein the last one of x corresponds to the 10th charge before the holding. Increasing irreversibility between dissolution and deposition is observed upon cycle.

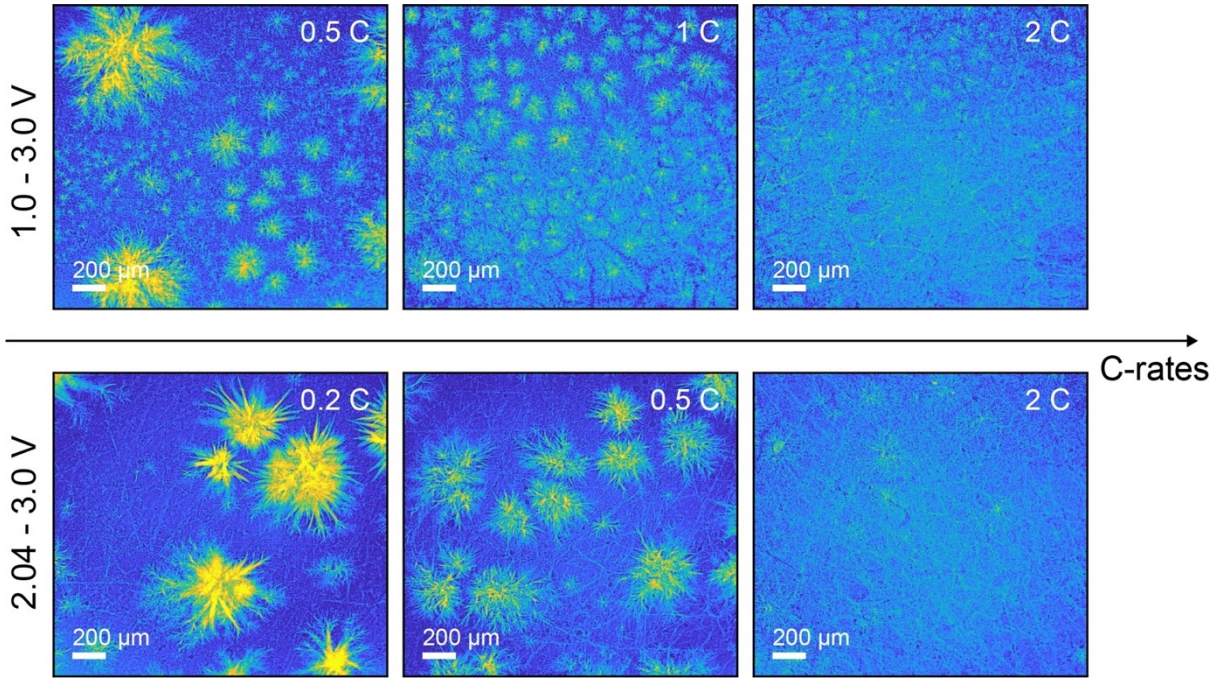

Fig. S22 Comparison of Se deposits with voltage ranges and charge current rates, delivering the nucleation-favored deposition at higher current rates even in the electrode of prevailing growth mode in 2.04-3.0 V.

Supplementary Video Captions

Video S1 *Operando* TXM of the Se dissolution and deposition reactions at 0.5 C in voltage range of 1.0-3.0 V.

Video S2 *Operando* XANES imaging at specific energy upon discharge and charge reactions, and chemical state mappings of Se and Li_2Se.

Video S3 CT of the deposited Se distributions and focusing the one dendritic Se deposit.

Video S4 *Operando* TXM of the Se dissolution and deposition reactions at relatively low Se loading of ~1 mg cm^{-2}.

Video S5 *Operando* TXM of the Se dissolution and deposition reactions at high charge current rates of 1 C and 2 C.

Video S6 *Operando* TXM of the Se dissolution and deposition reactions in upper voltage range of 2.04-3.0 V at 0.5 C for 10 cycles.

Video S7 *Operando* TXM of the Se dissolution and deposition reactions in upper voltage ranges at variable charge current rates.

Video S8 *Operando* TXM of the Se dissolution and deposition reactions in upper voltage ranges at high charge current rate of 2 C.

References for Supplementary Information

1. A. Bewick, M. Fleischmann and H. R. Thirsk, *Trans. Faraday Soc.*, 1962, **58**, 2200-2216.
2. B. Scharifker and G. Hills, *Electrochimica Acta*, 1983, **28**, 879-889.
3. Y. Cui, A. Abouimrane, J. Lu, T. Bolin, Y. Ren, W. Weng, C. Sun, V. A. Maroni, S. M. Heald and K. Amine, *J. Am. Chem. Soc.*, 2013, **135**, 8047-8056.
4. X. Ji and L. F. Nazar, *J. Mater. Chem.*, 2010, **20**, 9821-9826.
5. F. Y. Fan, W. C. Carter and Y.-M. Chiang, *Adv. Mater.*, 2015, **27**, 5203-5209.
6. H. G. Yang, C. H. Sun, S. Z. Qiao, J. Zou, G. Liu, S. C. Smith, H. M. Cheng and G. Q. Lu, *Nature*, 2008, **453**, 638-641.
7. C. Yang, X. Cui, Z. Zhang, S. W. Chiang, W. Lin, H. Duan, J. Li, F. Kang and C.-P. Wong, *Nat. Commun.*, 2015, **6**, 8150.
8. I. T. McCrum, M. A. Hickner and M. J. Janik, *Langmuir*, 2017, **33**, 7043-7052.